Modeling of Water Sorption and Swelling in Polymer Electrolyte Membranes:

Diagnostic Applications

by

Motahareh Safiollah
B.Sc., Sharif University of Technology, 2011

Thesis Submitted in Partial Fulfillment
of the Requirements for the Degree of

Master of Science

in the
Department of Chemistry
Faculty of Science

SIMON FRASER UNIVERSITY
Spring 2015

APPROVAL

Name: Motahareh Safiollah

Degree: Master of Science

Title of Thesis: Modeling of Water Sorption and Swelling in Polymer Electrolyte Membranes: Diagnostic Applications

Examining Committee: Dr. Hua-Zhong (Hogan) Yu, Professor
Chair

Dr. Michael Eikerling,
Professor, Senior Supervisor

Dr. Erik Kjeang,
Assistant professor, Supervisor

Dr. Nancy Forde,
Associate professor, Supervisor

Dr. Gary Leach
Associate Professor, Internal Examiner

Date Approved: 23 April 2015

Partial Copyright Licence

Abstract

The polymer electrolyte membrane (PEM) fulfills vital functions as separator, proton conductor, and electronic insulator in a polymer electrolyte fuel cell (PEFC). The well-studied and practically used solid polymer electrolyte membranes are perfluorosulfonic acid (PFSA) polymer membranes such as Nafion. These membranes offer high proton conductivity, high mechanical strength and good chemical stability. The efficiency of the chemical-to-electrical energy conversion in a PEFC critically depends on the ability of the PEM to transport protons from the anode to the cathode. Proton conductivity of the PEM is a key parameter to achieve high power density and performance.

The main variable to characterize the state of a PEM and determine its transport properties is its water content. In particular, the proton conductivity is highly sensitive to the level of hydration. Membranes experience continuous stresses and consequently continuous loss of performance throughout their operational life. Chemical degradation alters the chemical structure of the PEM, which affects the water distribution in it. A consistent description of water sorption and swelling under conditions relevant for the PEFC operation lies at the heart of understanding transport properties, performance and degradation phenomena.

This work expands on a previously developed poroelectroelastic model of water sorption in PEMs [Soft Matter 7, 5976 (2011)]. The theory relates the charge density at the pore walls to a microscopic swelling parameter. Extended to the water sorption equilibrium in a pore ensemble, the model reconciles microscopic swelling in a single pore with macroscopic swelling of the membrane.

This work provides a generalized treatment of elastic effects in PEMs. Different deformation modes of polymeric pore walls are used to derive stress-strain relationships that determine the law of swelling. Moreover, this work enhances the diagnostic capabilities of the model; it provides the statistical pore size distribution as well as a statistical distribution of microscopic fluid and elastic pressures inside the PEM. Thereafter, the model is applied to different sets of water sorption data for PEMs that had undergone either hygrothermal aging or chemical degradation. The model-based analysis provides mechanistic explanations of structural changes and their impact on microscopic distributions of charge density and elastic properties in PEMs.

Keywords: Polymer electrolyte fuel cells, Polymer electrolyte membrane, Water sorption and

swelling, Membrane degradation, Polymer elasticity

Acknowledgments

First and foremost, I would like to sincerely thank my supervisor, Professor Michael Eikerling for his support and guidance. I am inspired by his enthusiasm and creativity and the value he places on honest scientific inquiry. I am grateful to him for providing me opportunity to participate in international conferences and workshops. He taught me how to think logically, read critically, research productively.

I also thank my committee members, Doctor Nancy Forde and Doctor Erik Kjeang for their support and advice. I am thankful to Doctor Peter Berg at Norwegian University of Science and Technology for scientific discussion he had with me which made my stay memorable there.

I thank all the current and past members of the Eikerling group for their friendship and collaboration. I am grateful to Alix, Anatoly, Tasleem, Swati, Ali, Heather, Jianfeng ,Karen, Ata and Liya for their friendship and their support. A special word of thanks is due for Alix with whom I had innumerable discussions and received useful advice.

I acknowledge the financial supports from Ballard Power System and Automotive Partnership Canada.

Finally, I would like to thank my parents and my brothers Mohammad and Hossein for their unconditional love and support and for believing in my potentials even at moment when I did not.

Contents

List of Tables

List of Figures

Acronyms

Acronym	Definition
AFC	Alkaline fuel cell
BET	Brunauer-Emmett-Teller
CLs	Catalyst layers
EW	Equivalent weight
FFs	Flow fields
FTIR	Time-dependent Fourier transform infrared
GDL	Gas diffusion layer
GAB	Guggenheim-Anderson-de Boer
HHV	Higher heating value
IR	Infrared and raman spectroscopy
IEC	Ion exchange capasity
LHV	Lower heating value
MPL	Microporous layer
MCFC	Molten carbonate fuel cell
NMR	Nuclear magnetic resonance
PEFCs	Polymer electrolyte fuel cells
PEM	Polymer electrolyte membrane
PTFE	Polytetrafluoroethylene
QENS	Quasi-elastic neutron scattering
SECM	Scanning electrochemical microscopy
SANS	Small angle neutron scattering
SAXS	Small angle X-ray scattering
SOFCs	Solid oxide fuel cells
sPEEKK	Sulfonated polyetherketone
XRD	X-ray powder diffraction
WAXS	Wide angle X-ray scattering

List of Symbols

Symbols	Definition
a_w	Activity of water
C_{H^+}	Proton concentration at the pore wall
E°_{eq}	Standard cell potential
F	Faraday constant
F^{el}	Free energy of deformation
G	Shear modulus
P^c	Capillary pressure
P^{el}	Elastic pressure
P^{fl}	Fluid pressure
P^g	Gas pressure
P^l	Liquid pressure
P^l_{ext}	External liquid pressure
P^{osm}	Osmotic pressure
P^s	Saturated vapour pressure
P^v	Vapour pressure
L	Length of the pore
N_{uc}	Number of unit cells
R_0	Reference radius of the pore
R_c	Capillary radius
R_g	Gas constant
r_B	Radius of the bundle
r_r	Radius of the rod
RH	Relative humidity
T	Temperature
u	Velocity
$\bar{V_w}$	Molar volume of water
V_0	Volume on non-swollen network
$\bar{V_p}$	Molar volume of polymer
X_w	Water volume fraction
W_e	Electrical work
W_r	Reversible work

Greek symbols	Definition
α	Reorganization parameter
β_{ij}	Components of the deformation tensor
$\bar{\bar{\beta}}$	Deformation tensor
γ	Surface tension of water in pores
ΔH°	Enthalpy of the reaction
ΔS	Entropy change
ΔG_s	Gibbs energy of water sorption
ΔG	Gibbs free energy change
ΔG_w	Gibbs free energy of water
ΔS	Entropy change of the reaction
$\frac{\Delta V}{V_0}$	Volumetric expansion of the membrane
ε_0	Vacuum dielectric permittivity
ε_{carnot}	Carnot efficiency
ε_r	Dielectric permittivity
η	Swelling parameter
θ	Contact angle
λ	Water content
${\mu^{PEM}}_W$	Chemical equilibrium of the water in PEM
${\mu^{ext}}_W$	Chemical equilibrium of the water in the external vapour phase
μ	Viscosity
ν_0	Volume of a unit cell
ρ_p	Polymer density
$\rho_{SO_3{}^-}$	Density of surface charges
σ_0	Surface charge density
${\sigma_0}^{max}$	Maximal wall charge density
$\bar{\sigma_0}$	Average surface charge density
n(σ_0)	Statistical surface charge density distribution
ϕ_p	Volume fraction of polymer
ϕ	Potential
χ	Adjustable parameter in Flory-Huggins Solution theory

Chapter 1

Introduction

1.1 The History of Fuel Cells

The history of fuel cells goes back to the early nineteenth century. The discovery and first demonstrations of the fuel cell principle were made by Christian Friedrich Schoenbein and Sir William Grove. Grove conducted a series of experiments, by which he ultimately proved that electric current could be produced from an electrochemical reaction between hydrogen and oxygen over a platinum catalyst. His electrolysis/fuel cell system using platinum electrodes is shown in Figure 1.1. The term fuel cell was coined in 1889 by Charles Langer and Ludwig Mond, who researched fuel cells using coal gas as a fuel [18].

In the early twentieth century, several attempts were made to put fuel cells into practice. In 1959, Francis Bacon developed a practical 5kW fuel cell system, an alkaline fuel cell. Harry Karl Ihrig fitted a modified version of the Bacon cell into an Allis-Chalmers agricultural tractor [2]. This was one of the first practical implementations of fuel cells (Figure 1.2).

In the 1960s, NASA, in collaboration with industrial partners, made a series of developments in this area. Willard Thomas Grubb at General Electric is credited with invention of polymer electrolyte fuel cells (PEFCs); the first patent on this technology in 1959 was issued in his name [44]. He continued this development together with Leonard Niedrach, another researcher at General Electric. The Grubb-Niedrach cell was developed in collaboration with NASA for the Gemini space program. Similar programs in fuel cell development for space missions were pursued in the former Soviet Union. International Fuel Cells developed a 1.5 kW alkaline fuel cell (AFC) that was used in the Apollo space missions, providing electrical power and drinking water for the astronauts for the duration of the mission [2, 43].

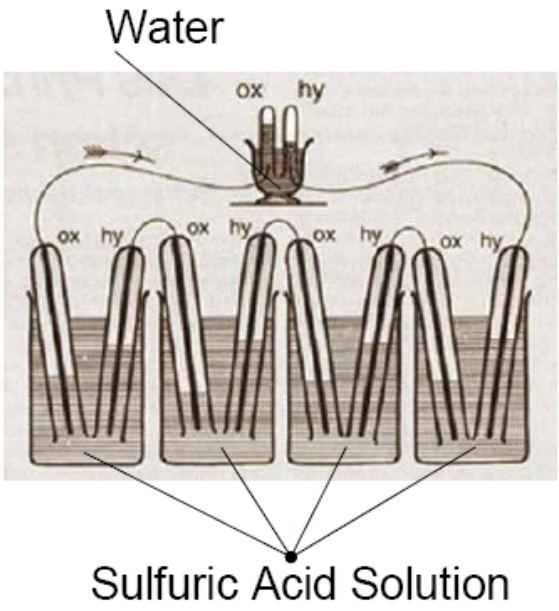

Figure 1.1: William Grove's fuel cell - gaseous voltaic battery - from 1839. The lower part of this image consists of four fuel cells that supply current to the electrolytic cell, placed above the fuel cells, in order to perform electrolysis of water.

About two centuries after their discovery, the high efficiency and low emission render fuel cells strong candidates for a revolution in power generation. There are many companies and research institutes investing their resources into research and development of different types of fuel cells for various applications. Cars, buses, motorcycles, trucks, forklifts, and even aircrafts, ships and trains are targeted by fuel cell developers. Thousands of stationary fuel cell systems have been installed worldwide in offices, schools, hospitals and remote or isolated areas [2]. A recent report, published in 2013 [101], predicts a marked increase in the demand for fuel cell systems as illustrated in Figure 1.3.

1.2 The Global Energy Challenge

In 2008, 87 % of the world′s primary energy demand was supplied from non-renewable sources [67]. However, the global energy infrastructure is undergoing a dramatic transition because the

Figure 1.2: Allis-Chambers tractor using 1008 fuel cells for power. (Photo courtesy of Smithsonian Science Service)

main product of the combustion process, CO_2, is a greenhouse gas and contributes significantly to the global warming phenomenon. Therefore, the search for advanced energy conversion technologies has become a foremost global concern. Awareness of this situation drives a growing number of international initiatives to develop renewable energy technologies, relying both on alternative primary energy sources (bioenergy, solar energy, wind and hydro power), and electrochemical secondary sources (fuel cells, batteries and supercapacitors).

The electrochemical reaction of hydrogen with oxygen produces water and generates electricity. Fuel cells for the propulsion of vehicles are highly efficient and potentially sustainable options for the future of transportation, which could drastically reduce health and environmental concerns.

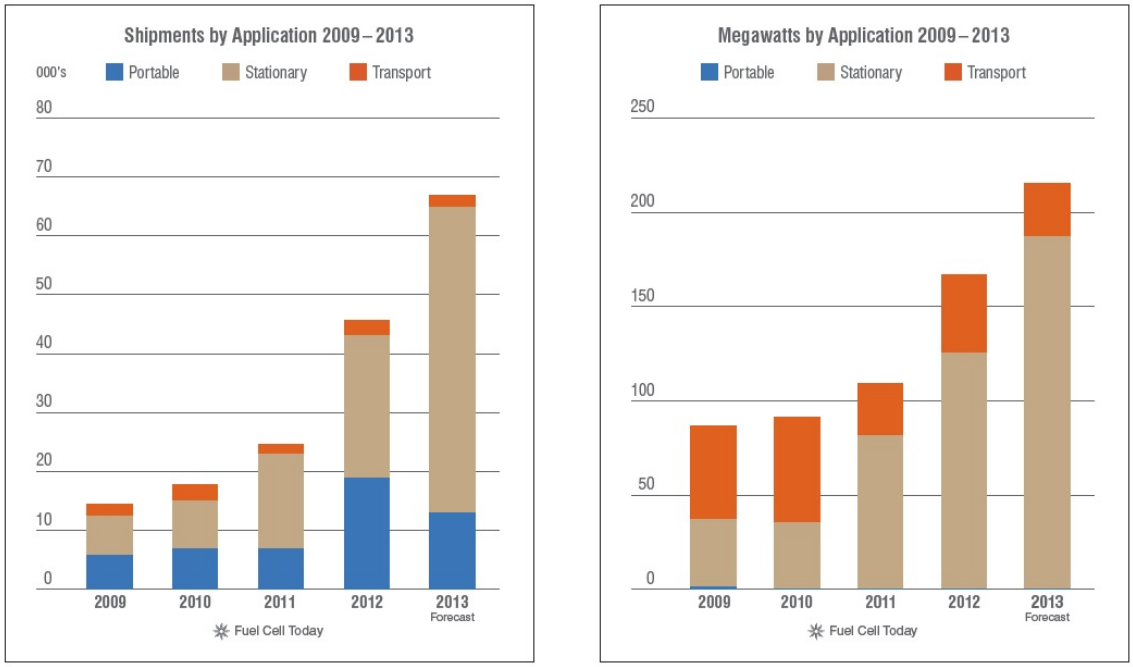

Figure 1.3: Fuel cell systems demand in 2009-2013 [101]

1.3 Overview of Fuel Cell Technologies

A fuel cell is a device that converts the chemical energy from a hydrogen-rich fuel into electricity through a chemical reaction with oxygen or another oxidizing agent. Fuel cells are made up of three basic components, which form a layered structure: anode, electrolyte, and cathode. Partial redox reactions occur at the electrode/electrolyte interfaces. At the anode, hydrogen is oxidized

$$H_2(g) \rightarrow 2H^+(aq) + 2e^-, \tag{1.1}$$

and at the cathode, oxygen is reduced

$$O_2(g) + 4H^+(aq) + 4e^- \rightarrow 2H_2O(l). \tag{1.2}$$

The overall cell reaction is

$$2H_2(g) + O_2(g) \rightarrow 2H_2O(l). \tag{1.3}$$

The net result of the two reactions is that the fuel is consumed, water is created, and an electrical current is generated, which can be used to power electrical devices [15].

There are various criteria to distinguish various fuel cell types. The most common classification schemes employ differences in electrode material, fuel and operating temperature. A widely used classification scheme is presented in Table 1.4. Depending on the operating temperature, two main groups of fuel cells exist.

High-temperature fuel cells such as solid oxide fuel cells (SOFC) and molten carbonate fuel cells (MCFC) can be fed with a variety of fuels, such as hydrogen, natural gas or carbon monoxide from gasified coal [4]. The operating temperature is between 500 °C to 1000 °C for SOFCs and above 650 °C for MCFCs. Recent advances in fabrication techniques have enabled lowering the temperature range of SOFCs to 650-850 °C [89] without compromising cell efficiency. The high temperature is essential for the performance of the SOFCs electrolyte, which is usually a ceramic material that conducts oxygen ions. The ionic conductivity of the electrolyte decreases at low temperatures, which leads to an increase in the Ohmic resistance of the cell. The main applications of SOFC and MCFC are distributed power and backup power generation, and combined heat and power generation [3, 95].

Low-temperature fuel cells include alkaline fuel cells (AFCs) and polymer electrolyte fuel cells (PEFCs). The primary advantages of operating under low temperature include more rapid start-up and higher efficiency [15]. However, low-temperature operation generally requires more expensive catalysts and larger heat exchangers to eliminate waste heat due to the low temperature difference with the environment. AFCs suffer from intolerance to even small fractions of air carbon dioxide (CO_2) that react to form potassium carbonate in the electrolyte and reduce its performance over time. The requirement of pure H_2 and the sensitivity to CO_2 appear to be among the major factors limiting the widespread application of AFCs.

The use of a solid polymer electrolyte eliminates the corrosion and safety concerns associated with liquid electrolyte fuel cells. PEFCs operate at temperatures below 100 °C. The low operating temperature provides instant start-up and requires no thermal shielding. Recent advances in performance and design offer the possibility of lower cost than any other fuel cell system. However, they have mainly been developed for vehicular, most importantly fuel cell powered automobiles and heavy-duty buses.

Fuel Cell Type	Electrolyte Material	Operating Temperature (◦C)	Major Poison	Advantages	Disadvantages	Most Promising Applications
Alkaline fuel cell	Solution of potassium hydroxide in water	60–250	CO_2	High efficiency, low oxygen reduction reaction losses	Must run on pure oxygen without CO_2 contaminant	Space applications with pure O2/H2 available
Phosphoric acid fuel cell	Solution of phosphoric acid in porous silicon carbide matrix	160–220	Sulfur, high levels of CO 1–2% CO tolerant	Good-quality waste heat, demonstrated durability	Low power density, expensive, platinum catalyst used, slow start-up, loss of electrolyte	Premium stationary power
Solid oxide fuel cell	Yittria (Y_2O_2) stabilized zirconia (ZrO_2)	600–1000	Sulfur, CO tolerant	Fuel flexible, high-quality waste heat, inexpensive catalyst	Long start-up time, durability under thermal cycling, inactivity of electrolyte below ∼600◦C	Stationary power with cogeneration, continuous-power applications
Molten Carbonate fuel cell	Molten alkali metal (Li/K or Li/Na) carbonates in porous matrix	600–800	Sulfur CO tolerant	Fuel flexible, high-quality waste heat, inexpensive catalyst	Electrolyte dissolves cathode catalyst, long start-up time, electrolyte maintenance	Stationary power With cogeneration, continuous-power applications
Polymer Electrolyte fuel cell	Flexible solid perfluorosulfoni acid polymer	30–100	CO, Sulfur, metal ions, peroxide	Low-temperature operation, high efficiency, high H_2 power density, relatively rapid start-up	Expensive catalyst, durability of components not yet sufficient, poor-quality waste heat, Intolerance to CO, thermal and water management	Portable, automotive, and stationary applications

Figure 1.4: Fuel cell types and description; adopted from Ref. [65].

1.3.1 Polymer Electrolyte Fuel Cells (PEFCs)

PEFCs use hydrogen as the fuel in the anode, and oxygen in the cathode, producing only water as a chemical product and generating electricity. Figure 1.5 shows the schematic of a membrane electrode assembly in a PEFC. The electrodes consist of 1) catalyst layers (CLs), 2) gas diffusion layers, GDL, and, 3) gas flow fields (FFs). Often times, at the cathode side, a microporous layer (MPL) is included between CL and GDL in order to facilitate the removal of product water from the cathode CL.

During operation hydrogen gas is transported through flow channels to the porous gas diffusion layer (GDL). After diffusion through the GDL, it flows into the anode catalyst layer. At the anode catalyst, H_2 is oxidized into protons (H^+) and electrons,

$$H_2(g) \rightarrow 2H^+(aq) + 2e^-. \tag{1.4}$$

The membrane is an electric insulator. It forces electrons to flow in an external electric circuit. At the cathode, oxygen reacts with protons and electrons to produce water,

$$O_2(g) + 4H^+(aq) + 4e^- \rightarrow 2H_2O(l). \tag{1.5}$$

The overall cell reaction is

$$2H_2(g) + O_2(g) \rightarrow 2H_2O(l). \tag{1.6}$$

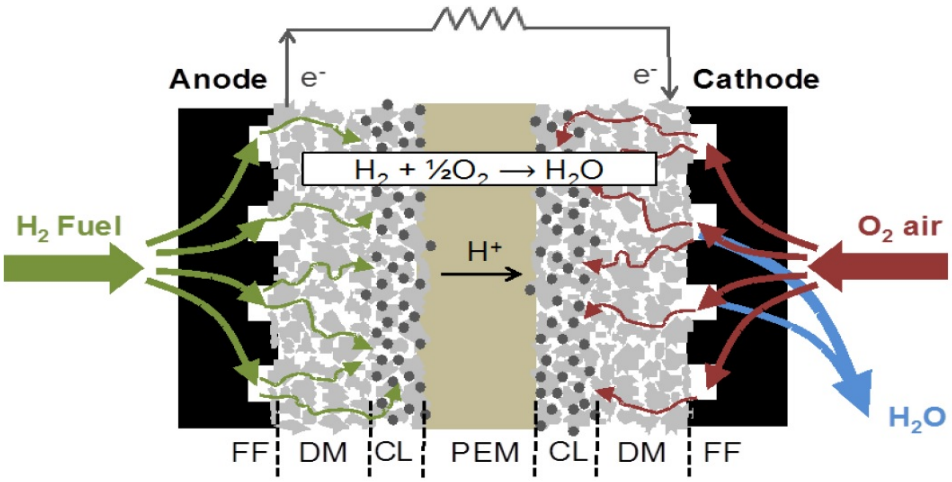

Figure 1.5: Schematic of a PEFC; FF = flow field, DM = diffusion media, CL = catalyst layer, PEM = polymer electrolyte membrane

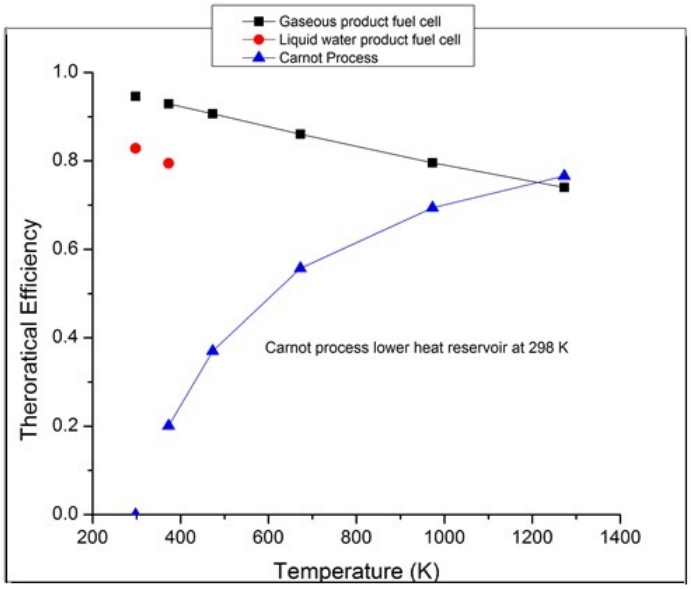

Figure 1.6: Thermodynamic efficiencies of a fuel cell and a hypothetical Carnot heat engine, plotted as a function of temperature. A fuel cell that forms water in a gaseous phase has a higher efficiency compared to a fuel cell that produces liquid water. The efficiency difference corresponds to the enthalpy of vaporization [18].

The reaction Gibbs energy change of this process is $\Delta G = -237kJ/mol$. The standard cell potential is

$$E^0_{eq} = \frac{-\Delta G}{2F} = 1.23V \tag{1.7}$$

where F is the Faraday constant.

The high reversible efficiency is one of the major advantages of PEFCs. The thermodynamic efficiency of a heat engine is limited by ideal reversible efficiency of the the Carnot cycle,

$$\varepsilon_{carnot} = \frac{-W_r}{\Delta H^\circ} = 1 - \frac{T_2}{T_1} \tag{1.8}$$

where W_r is the reversible work, ΔH° is the enthalpy of the reaction, and T_1 and T_2 are temperatures of hot and cold reservoirs. For highly efficient engines at practical operating temperatures, ε_{carnot} does not exceed 50%.

In a fuel cell the reversible efficiency is,

$$\varepsilon_{FC} = -\frac{W_e}{\Delta H^\circ} = \frac{\Delta G^\circ}{\Delta H^\circ} = \frac{\Delta H^\circ - T\Delta S^\circ}{\Delta H^\circ}, \tag{1.9}$$

where W_e is the electrical work, ΔH° the enthalpy of the reaction, ΔG° is the Gibbs energy of the reaction, and $T\Delta S^\circ$ corresponds to the reversible heat of the reaction; ΔH° = -286 kJ mol^{-1}. This enthalpy value is based on the higher heating value (HHV) i.e. when liquid water is produced in the reaction. If however, the product water is in vapor phase then the reaction enthalpy is based on the lower heating value (LHV) and is equal to -242 kJ mol^{-1}. The standard Gibbs free energy of the fuel cell reaction is ΔG° = -237 kJ mol^{-1} based on the HHV and -229 kJ mol^{-1}, based on the LHV. Thus Equation 1.9 gives a theoretical efficiency of 83%, based on liquid water production, and 94% based on vapour water production. Thermodynamic efficiencies of a fuel cell and a hypothetical Carnot heat engine are plotted as a function of temperature in Figure 1.6. However, the practical efficiency is lower due to activation, ohmic and mass transport losses that occur in an operating fuel cell. In general, the operating voltage of a fuel cell can be represented as the departure from the equilibrium cell voltage E^{eq},

$$E^{cell} = E^{eq} - \eta_{a,a} - |\eta_{a,c}| - \eta_r - \eta_{m,a} - |\eta_{m,c}| - \eta_x, \tag{1.10}$$

where $E^{eq}(T, P)$ is the theoretical equilibrium open-circuit potential of the cell, calculated from the Nernst equation. The activation overpotentials at the anode and cathode are represented by $\eta_{a,a}$ and $\eta_{a,c}$, respectively. Crossover of fuel and oxidizer through the electrolyte results in an over voltage η_x. The ohmic polarization is denoted as η_r. Concentration (mass transfer) polarization at the anode and cathode are represented as $\eta_{m,a}$ and $\eta_{m,c}$, respectively. The resulting typical efficiency of fuel cell is about 50 - 60 %.

On one hand, to increase the practical efficiency, fuel cells should operate at elevated temperatures; however above 90 $^\circ$C it is difficult to maintain the proper level of hydration in the PEM. Water management is one the most important issues in fuel cell operation; excess water in the cell causes mass transport losses due to flooding of the porous diffusion media, which should provide gas pores for diffusion of H_2 at the anode side and O_2 at the cathode side. Conversely, too little water significantly decreases the proton conductivity within the membrane and catalyst layers. During operation, expansion and contraction of the PEM because of varying hydration level can cause loss of contact with the electrodes. Moreover, cracks can form in the membrane, leading to gas crossover and associated voltage loss. Research efforts are ongoing to develop electrolyte materials that achieve high conductivity at elevated temperature (i.e. low hydration) as well as membranes with dimensional stability and fatigue resistance.

1.3.2 Polymer Electrolyte Membrane (PEM)

The term polymer electrolyte is used to describe polymer-based materials with significant ionic conductivity. The polymer electrolyte membrane (PEM) is the heart of a PEFC. The PEM fulfills

vital functions as a separator medium, proton conductor, and electronic insulator. Therefore, PEMs must be optimized in view of their

- proton conductivity,
- mechanical, chemical and thermal strength,
- suppressed gas permeability,
- reduced electro-osmotic drag.

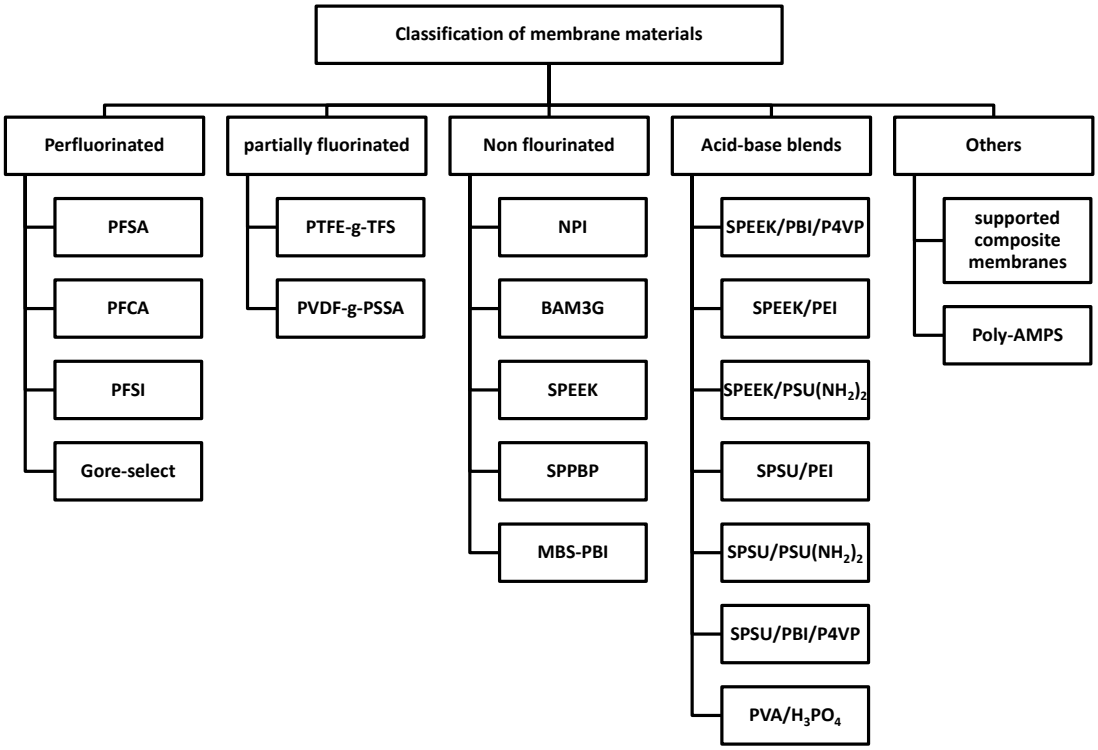

Figure 1.7: Classification of membrane materials [91].

The evolution of polymer membranes for fuel cell applications started with the testing of phenolic membranes by GE in 1959. The problem of these membranes was their low mechanical strength, a short lifetime of $300-1000$ h, and a low power density of $0.05-0.1$ kW m^2 [60]. During $1962-1965$, GE attempted to improve the power density by developing partially sulfonated polystyrene sulfonic

acid membranes. These membranes exhibited a better water uptake and an improved power density of $0.4-0.6$kW m^2 that enabled their application in NASAs Gemini flights [6].

The main problem with membranes of that time was their low proton conductivity, which was barely able to reach a power density of 100 mW cm^2 [96].

Figure 1.7 gives the classification of the membrane materials used in PEFCs. Membrane materials fall into different categories, which can be classified as:

- **perfluorinated ionomers:** Du Pont developed a perfluorosulfonic acid membrane called Nafion® in the 1970s. These membranes not only showed a two-fold increase in the specific conductivity but also an extended lifetime (up to 60,000 h). They have good mechanical, chemical and thermal strength because of their PTFE backbone and relatively low equivalent weight. Their proton conductivity in well hydrated conditions is $0.1-0.2$ S cm^{-1} at PEFC operating temperatures.
- **partially fluorinated polymers:** Compared to perfluorinated ionomers, these membranes degrade faster and have a lower performance.
- **non-fluorinated hydrocarbons:** These membranes, in spite of their good mechanical strength, have poor chemical and thermal stability as well as poor proton conductivity.
- **non-fluorinated membranes with aromatic backbone:** These membranes are mechanically, chemically, and thermally stable and they exhibit good water sorption. They also have relatively high proton conductivity. However, compared to perfluorinated ionomers, they show lower proton conductivity. As an example, the microstructures of sulfonated polyetherketone (sPEEKK) and Nafion are compared in Figure 1.8. Nafion has wider, more separated, less branched channels with good connectivity that confer higher conductivity.
- **acid-base blends:** These membranes are stable in oxidizing, reducing, and acidic environments. They exhibit proton conductivity comparable to Nafion but their durability is a problem.

It can be noticed that the perfluorinated ionomers, among which Nafion serves as a benchmark, possess most of the desired properties and hence appear to be most promising for fuel cell applications. Nafion is a poly(tetrafluoroethylene)-based random copolymer. It has a Teflon-like backbone and sulfonic acid -RSO_3H functional groups at the end of pendant side chains. The sulfonic groups fully dissociate in aqueous environments. The chemical structure of a PFSA ionomer like Nafion is shown in Figure 1.9.

This unique molecular structure of Nafion leads to the formation of connected proton-conducting pathways in the hydratred state [16, 62, 68, 73, 98]. The large difference in solubility of the highly

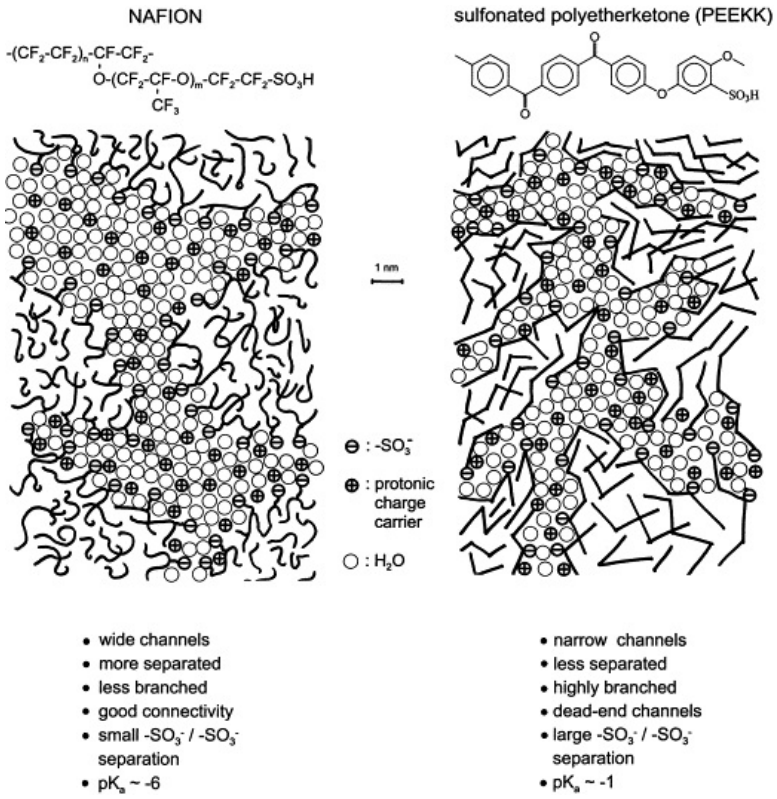

Figure 1.8: Schematic representation of the microstructures of Nafion and a sulfonated polyetherketone [54] illustrating the less pronounced hydrophobic/hydrophilic separation of the latter compared to the former.

hydrophobic perfluorinated backbone and of the strongly hydrophilic acid side chain head groups causes spontaneous aggregation of polymer backbones, which leads to a local phase-separation. When Nafion ionomer is exposed to liquid water or to a humid environment, the polymer self-organises into segregated domains of hydrophilic polar head groups and of hydrophobic parts. With increasing water uptake, a percolating network of water-filled pores forms and then undergoes continuous reorganization. The well-connected network of pores provides conductive pathways to transport protons throughout the film, while the perfluorinated backbone maintains the structural integrity of the film during hydration [52, 90]. Proton conductivity thus exhibits a pronounced dependence on water content as shown in Figure 1.10.

The parameter used to specify the ion content of a PEM is the ion exchange capacity (IEC). IEC is defined as the number of moles of ion exchange sites per mass of dry polymer. It determines the volumetric charge density (ρ_{H^+}) resulting from excess protons. It is also equal to the inverse of the equivalent weight (EW). The EW of Nafion can be calculated from the formula EW = (100 n + 444)

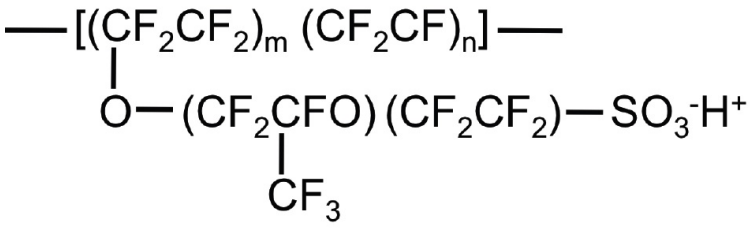

Figure 1.9: Chemical structure of Nafion

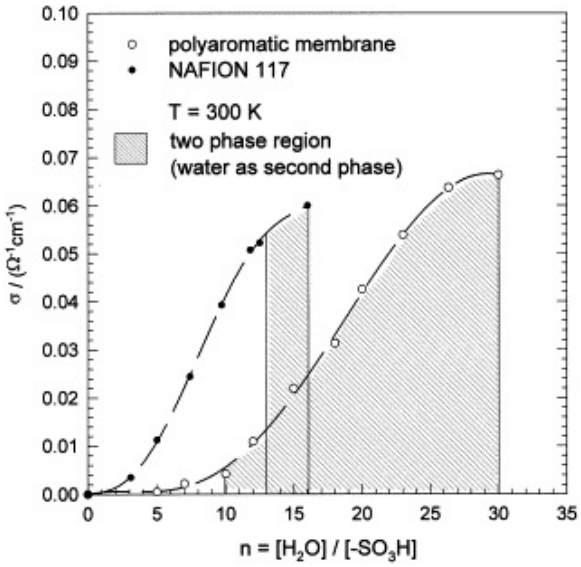

Figure 1.10: Effects of water content on conductivity [53]

g mol^{-1}. The first number, 100 g mol^{-1}, represents the molar mass of the TFE backbone monomer (CF_2CF_2), and n the average number of TFE monomers between neighboring side chains. The second term in brackets is the molar mass of a single Nafion side chain ($C_7F_{13}O_5SH$), 444 g mol^{-1}. This number is different for ionomer materials with a different side chain chemistry.

1.3.3 Morphology of Polymer Electrolyte Membranes

Various experimental techniques such as small-angle and wide-angle X-ray scattering (SAXS, WAXS), small-angle neutron scattering (SANS) [31, 35, 41, 47, 79], quasi-elastic neutron scattering (QENS) [74, 75, 94], infrared (IR) and Raman spectroscopy [25, 45], time-dependent Fourier transform infrared (FTIR) spectroscopy [97], nuclear magnetic resonance (NMR) [59], scanning electrochemical microscopy (SECM) [66], and electrochemical impedance spectroscopy [1] have been employed to unravel the relation between membrane structure, water uptake, and transport properties.

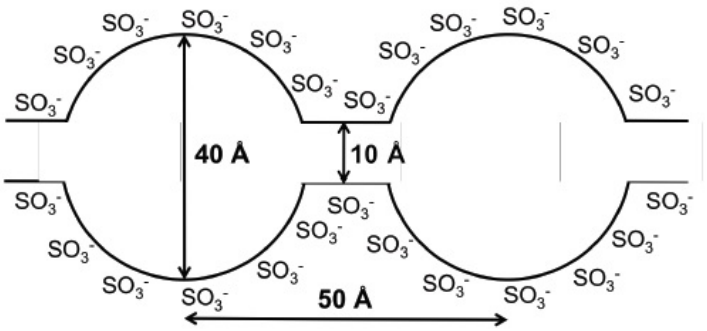

Figure 1.11: Schematic representation of Gierke model [41].

The cluster network model was proposed by Gierke et al [41] on the basis of small angle X-ray scattering (SAXS) data. This model suggested that water absorption leads to the formation of inverted micelles of about 4 nm diameter connected by narrow channels of $\sim$ 1 nm diameter, as shown in Figure 1.11. These sulfonic acid clusters are embedded into a hydrophobic polymer host. Although very simple, this model helped in understanding water fluxes and proton transport properties of Nafion in PEFC [22, 23].The weakness of the cluster-network model was its inability to describe the structural evolution of membranes over a wide range of humidification conditions, from the highly diluted polymer solution to the dry membrane state [23].

Another widely accepted model was proposed by Gebel *et al.* [33] These authors studied the structural evolution of the membrane as a function of water content. Upon absorption of water in the membrane, the isolated spheres of ionic clusters ($\sim$ 1.5 nm in diameter and a center-to-center separation distance of $\sim$2.7 nm) begin to swell. As shown in Figure 1.12, a percolation threshold is reached at a water volume fraction $X_w \sim 0.1$. At $X_w > 0.5$, a morphological inversion occurs such that the structure resembles a connected network of rods. The increasing water content of the

membrane is accompanied by an increase in the proton conductivity. On increasing X_w from 0.5 to 0.9, the conductivity of the membrane approaches the value observed for Nafion solution.

Although these studies gave valuable information, they cannot conclusively determine the microscopic and mesoscopic structure of the membrane. There is theoretical as well as experimental evidence that cylindrical fibres or bundles form the prevailing structural motif at the microscopic scale [58, 64, 83].

These fibres define electrostatic and elastic properties of the PEM. They can assemble further into superstructures. Structural models differ in terms of the shape of pores [54]. The main types consider cylindrical pores [34, 82, 83, 86], cage-like structures with spherical water-inclusions [50] and lamelar-like flat pore structures [55]. Figure 1.13 illustrates the main steps in the spontaneous structure formation from ionomer molecule to bundle and to different superstructures.

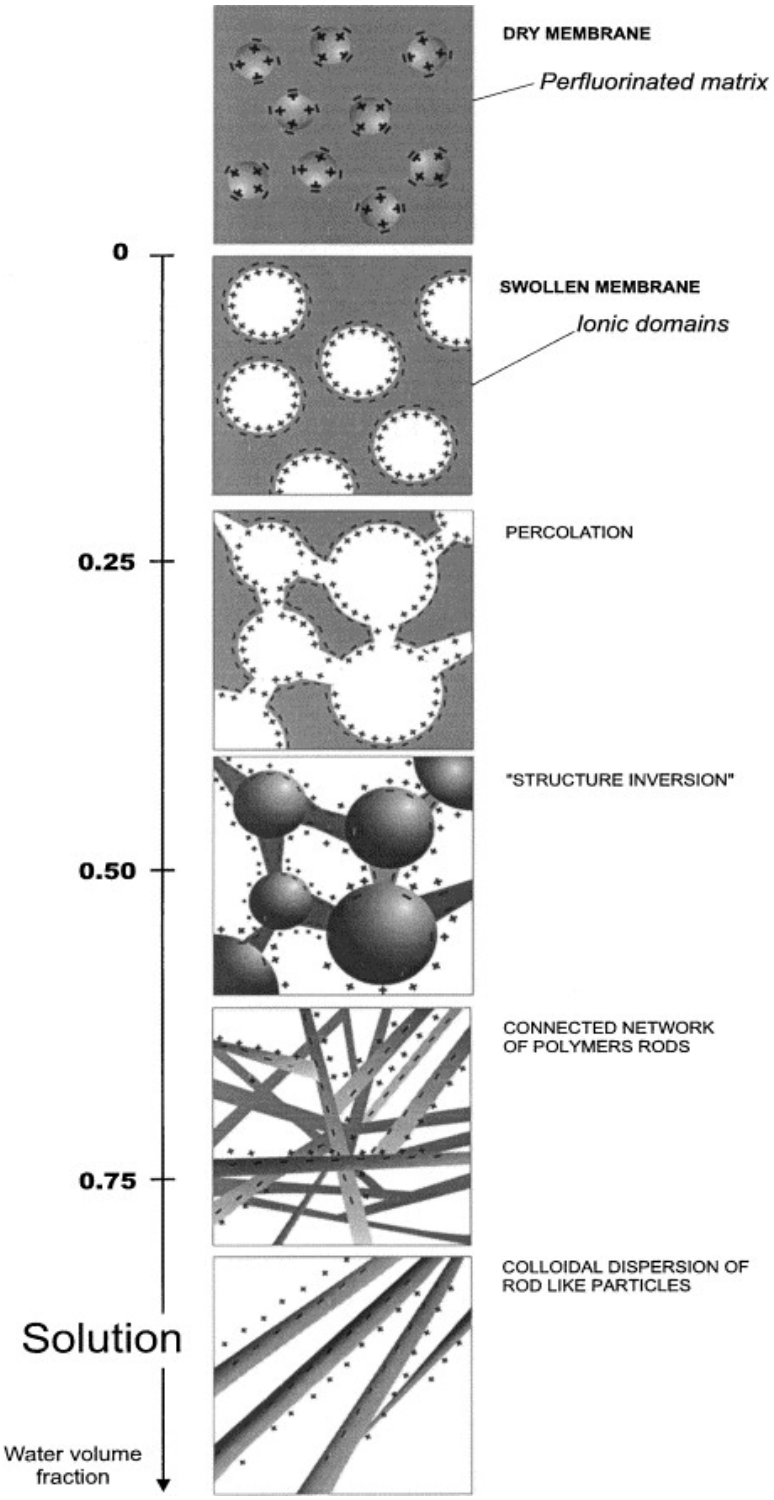

Figure 1.12: Structural evolution model proposed by Gebel [33]

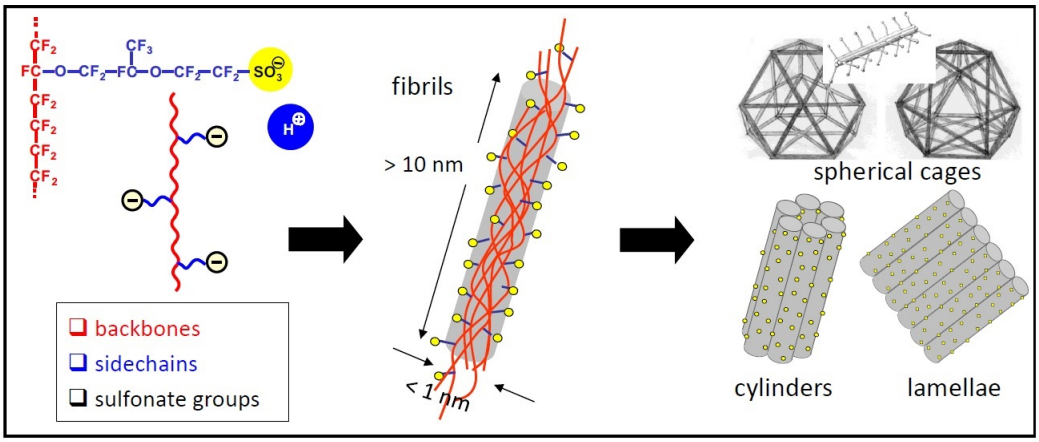

Figure 1.13: Structure formation from bundles of ionomers [50] to different super structures confining pores: cylindrical aggregates [86], lamellar structures, and spherical cages [50].

1.4 Challenges for the Operation of PEFC

Despite great advances in PEFC technology, there are still many scientific challenges associated with improving the performance of PEFCs including water management, material cost, degradation, and operating temperature. As they are related to the theme of this thesis, degradation and water management will be discussed in more detail in this section.

1.4.1 Degradation

Durability of PEFCs has been a major concern in industry. The membrane is shown to be one of the most vulnerable components. It predominantly determines the lifetime of a PEFC in heavy-duty bus applications. A combination of mechanical and chemical factors including harsh and rapidly varying operating conditions of PEFCs has a negative impact on the membrane lifetime.

Due to its nature, the membrane suffers from early stage performance degradation, leading to failure times less than the demanded value. Evidence of membrane degradation has been found after a few hundred to a few thousand hours of operation depending on the working conditions. The membrane becomes thinner and pinholes develop. Such pinholes result in high rates of hydrogen crossover and rapid performance decay, even failure of the whole cell in the worst case. Therefore, an important issue to achieve the lifetime targets of fuel cell industry would be the stability and

durability of the membrane.

The detailed mechanisms of membrane degradation are not fully understood. Chemical degradation is generally accepted as the key contributor to membrane degradation. The membrane is sandwiched between the highly oxidizing environment of the cathode and the reducing environment of the anode. Highly active chemical species, called radicals [11], play a major role in the process of membrane chemical degradation [11, 85, 88]. They attack the polymer structure leading to irreversible damage. Radicals can form on the anode side, cathode side, or even in the membrane [76, 103]. They can be the product of direct chemical or electrochemical reactions, or they can be the outcome of an intermediate species decomposition. Chemical degradation occurs predominantly through radical attack on main chain carboxylic acid groups [12, 38, 109], or on the C-S or O-C bonds of the side chain [37, 38, 39, 109] as illustrated in Figure 1.14 . Newer generations of Nafion membranes have been chemically stabilized, i.e., the concentration of terminal carboxylic acid groups has been decreased to small levels [12, 109]. Consequently, their backbone is resistant to chemical attack by hydroxyl radicals. This leaves radical attack on the side chain as the sole mechanism of chemical degradation (Ghassemzadeh et al. [36]). It has been proposed that membrane chemical stability can be further improved by using polymers with shorter side chains.

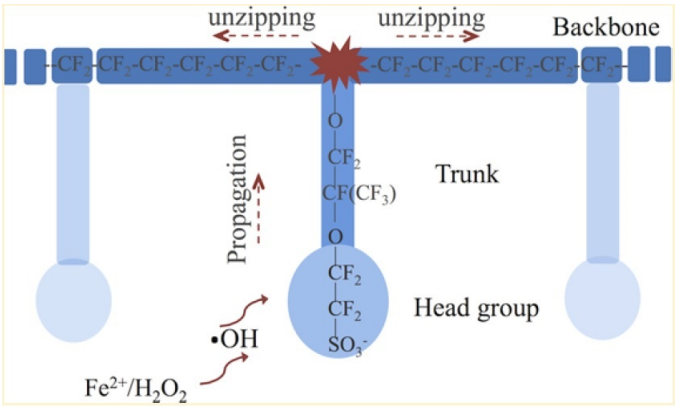

Figure 1.14: Coarse-grained representation of Nafion structure by headgroup, trunk, and backbone segments and attack of $OH^{\bullet}$ to the head group [40].

In contrast to mechanisms of chemical degradation that are responsible for the gradual deterioration of membrane properties, mechanical degradation has been identified as the major cause of sudden membrane failure. Cracks, tears, punctures and pinholes could cause a rapid drop in membrane performance. These defects act as shortcuts for reactant gases to reach the opposing side and react on the catalyst surface. This would decrease the cell voltage while the heat of these reactions can lead to local overheating and melting of the membrane.

Local high-stress areas, caused by manufacturing imperfections and even the penetration of catalyst particles into the ionomer, are the starting points of the evolution of holes in the membrane [11]. Inadequate humidification will make the membrane brittle and fragile, making it more susceptible to failure modes mechanical stress. X-ray powder diffraction (XRD) analysis of the degradation process in Nafion has shown that insufficient water in the membrane during operation would destroy the membrane crystalline structure [49].

1.4.2 Water Management

Maintaining a high water content in the membrane is necessary to ensure the required proton conductivity. However, excess liquid water is associated with a variety of performance and durability problems. Proton migration is accompanied by a drag of water molecules from the anode to the cathode side, which is called electro-osmotic drag [21]. At the cathode side of the membrane-electrode assembly, oxygen is reduced electrochemically, forming water. Electro-osmotic drag together with electrochemical water production result in an accumulation of water at the cathode. On the other hand, there is a back flux of water from cathode to anode, driven by gradient in concentration, activity, or liquid pressure of water. The inevitable electro-osmotic flux has to be compensated by the back flux of water. The water distribution in PEMs that is generated in response to these driving forces decreases from cathode to anode. With increasing current density, the water distribution becomes more non-uniform. At high current densities, more water is produced and electro-osmotic drag of water to the cathode can dry the anode and flood the cathode. This phenomenon complicates the overall hydration mechanism of the electrolyte membrane. As a consequence, the overpotential of the membrane increases dramatically; this can lead to failure of the complete cell [19]. Therefore, maintaining adequate hydration is difficult as such mechanisms are strongly coupled and, in most cases, not easily predicted.

1.5 Scope of the Thesis

Herein, we build upon a previously introduced physical model of water sorption and swelling by Eikerling and Berg [17]. In the following, we first discuss the phenomenology of swelling by briefly reviewing the basics of the model in Section 3.1. One of the main challenges to address in this work is the relation between the swelling pressure and the microscopic swelling of a single pore, which will be presented in Section 3.3. In that section, we derive different stress-strain relationships of polymer walls based on different microscopic deformation scenarios.

Convolution of a single pore model with an ensemble model was proposed in the previous version of the model. Here, we provide a more systematic analysis in order to find the best surface charge density distribution function. In Section 3.4, we explore relations between macroscopic effective water sorption and swelling and statistical distributions of surface charges, microscopic pore size and pressure. In Chapter 4, we provide parametric studies and experimental comparisons. Diagnostic capabilities of the model are demonstrated in Section 4.2; from macroscopic sorption data, we extract microscopic structural information and thus propose a microscopic picture to explain the degradation and aging studies that we have analysed.

Chapter 2

Phenomenology of Water Sorption in PEMs

Water content is the main thermodynamic variable to characterize the state of a PEM; it determines structure formation and transport properties as well as mechanical response and durability of the membrane. A consistent description of water sorption and swelling under relevant conditions of fuel cell operation is thus essential for the understanding of membrane performance and durability.

2.1 Experimental Water Sorption Studies in PEMs

The experimental basis of sorption studies includes isopiestic vapor sorption isotherms [77, 104], and capillary isotherms, measured by the method of standard porosimetry [14, 93].

In isopiestic vapor sorption experiment, the membranes are first pretreated using a well-established pretreatment procedure including boiling in H_2O_2, rinsing in boiling water, boiling in H_2SO_4, and finally rinsing in boiling water. Membranes are dried using certain protocols. The desired relative humidity is produced by the mixing ratio between the saturated vapour stream and the diluting nitrogen stream. To determine the vapour uptake at each state of hydration, membranes are removed from the chamber, blotted dry or shaken to remove excess surface water, and quickly weighed in a closed chamber. The membrane is then dried completely, and the water uptake is determined from the difference between dry and wet weights. An important issue is to let the membrane to equilibrate for enough time before removal from the chamber [77, 104].

The method of standard porosimetry is based on the laws of capillary equilibrium. This technique measures the equilibrium dependence of the relative liquid content in the test sample as a function of the volume of the liquid in standard sample.

Although, these methods give us valuable empirical insights into the structural evolution upon water uptake and the transport properties, they provide a limited theoretical understanding of how chemical structure effects physiochemical properties and electrochemical performance. We need physical models which are predictable in order to understand the sorption and swelling behaviour of the membrane under different operating conditions.

2.1.1 Schröeder's Paradox

One of the controversial phenomena observed in sorption of proton-exchange membranes is that there is a difference in solvent uptake when a sample is exposed to a saturated vapour versus a pure liquid. This so-called "Schröeder's paradox", remains a mysterious phenomenon in polymer science that has not yet been satisfactorily explained.

In 1903, von Schröeder in Ostwald's laboratory reported very interesting phenomenon that a piece of gelatin apparently did not reach the same equilibrium point in the presence of saturated vapour that it did when immersed in liquid water. This phenomenon has been associated with the failure of achieving the same temperature in the saturated vapour as in the liquid phase [69, 102], the low permeation rate of vapour phase adsorption [30], the insufficient time of vapour adsorption [102] and the poor wetting of the condensates on solid substances [105]. However, these different interpretations do not provide a general explanation of the phenomenon.

The difference in liquid versus vapour sorption is also observed in proton-exchange membranes as well [99, 100, 104, 105]. Since the proton conductivity in the membrane depends strongly on the amount of water in Nafion, the sorption characteristics of water and explaining the Schröeder's paradox are important in determining fuel cell performance. Some people explained it by assuming the hydrophobic nature for the PEM, which makes water uptake difficult when it contacts with vapour. Recently, Freger *et al.* [29] reported a difference in sorption amounts when sulfonated polyethylene polymer is contacted with different phases. Although a definite explanation for the reason is still not available, it is suggested that the effect was probably because of the changes in interfacial energies between the solvent and matrix phase [105].

Therefore, it is necessary to understand this intriguing phenomenon in proton-exchange membranes for designing high proton-conducting membranes and for optimizing the operation conditions for fuel cell. This will be addressed in this thesis.

2.2 Models of Water Sorption

Many sorption models have been developed for understanding the water sorption of the PEMs. The water sorption isotherms of ionomer membranes have generally a sigmoid shape; it is concave to the water activity at low relative humidity and convex to the same axis at high relative humidity. The

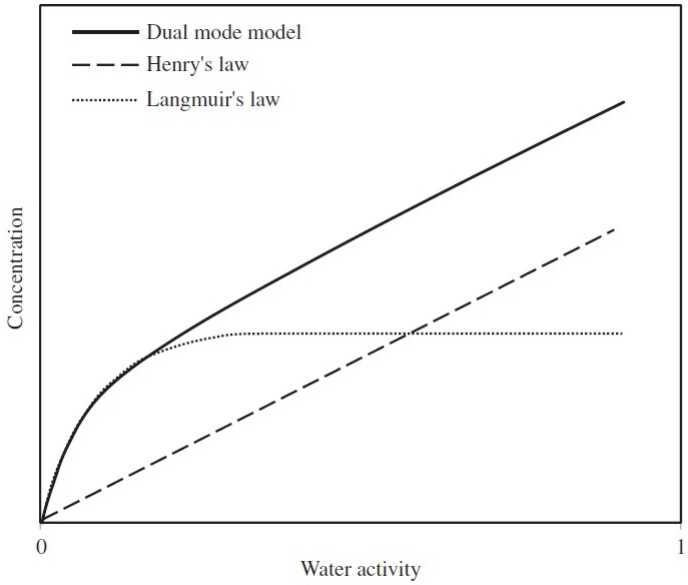

Figure 2.1: Type 1 sorption isotherm in glassy polymers: dual mode isotherm which is the combination of Langmuir and Henry isotherms [57].

observed sigmoid-shape isotherm has been simulated by different empirical models, which can be categorized in three main types.

2.2.1 Type 1: Dual Mode Sorption Model

In this model, the isotherm is concave to the activity axis at low activities and almost linear at higher activities, which is a combination of Langmuir and Henry isotherms as illustrated in Figure 2.1. This model assumes that penetrating water molecules are divided into two distinct populations that are in dynamic equilibrium with each other: first, the penetrant molecules are sorbed on specific sites (Langmuir's population) that are mainly microvoids in the glassy matrix and second, the penetrant molecules are sorbed by a dissolution mechanism in the dense polymer matrix (Henry's law population).

2.2.2 Type 2: The Sigmoid Sorption Isotherm

This category includes Brunauer-Emmett-Teller (BET) type II, Guggenheim-Anderson-de Boer (GAB) and Park models. Figure 2.2 shows a typical isotherm for type two sorption.

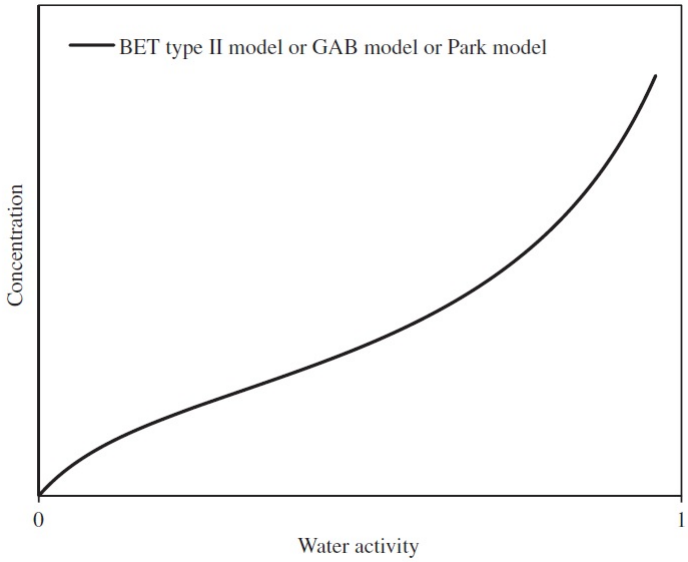

Figure 2.2: Type 2 sorption isotherm in glassy polymers [57].

BET Type 2

The BET type II is a combination of Langmuir (the first part of the curve, i.e. concave to the activity axis) and Flory-Huggins isotherms (the second part, i.e. convex to the activity axis) [13]. The BET model considers that water molecules condense in several layers on adsorption surfaces and assumes that beyond the second layer, their evaporation-condensation properties are the same as in the liquid state. However, this model is limited to water activity up to about 0.4-0.5.

GAB Model

The GAB sorption isotherm represents a refined extension of the Langmuir and BET theories. The theoretical basis for the GAB sorption isotherm is the assumption of localised physical adsorption in multilayers with no lateral interactions. The first shell of water evenly covers the sorbent surface and is very tightly bound in a monolayer. Subsequent layers of water have less interaction with the sorbent surface. The molecules in this so called multilayer (layers 2-9) have interactions with the sorbent, which range in energy levels somewhere between those of the monolayer molecules and the bulk liquid. Succeeding layers of water molecules exhibit more and more bulk liquid properties.

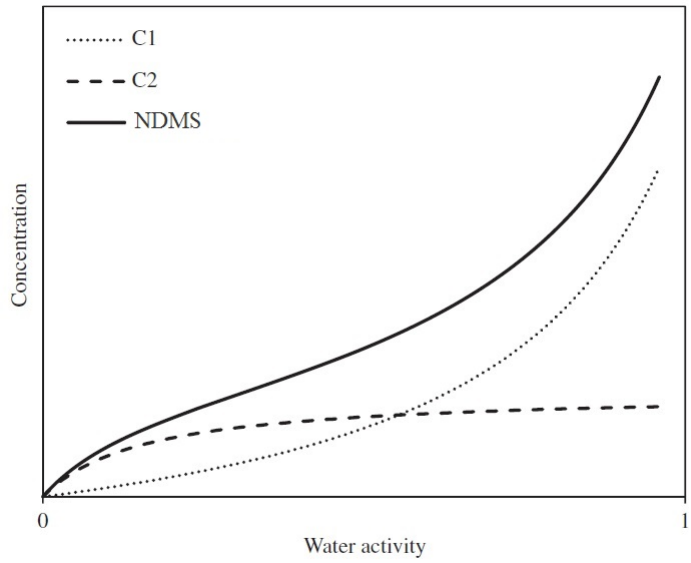

Figure 2.3: Schematic representation of the new dual model sorption (NDMS) model [57].

Park Model

The Park model for sigmoidal isotherms of water vapour considers three main mechanisms: Langmuir sorption on special sites (the first part of the curve), non-specific sorption of Henry's type (the second part) and water-molecule aggregation or clustering (the third part, i.e. convex to the activity axis) at high water activity based on the equilibrium $nH_2O \rightarrow (H_2O)_n$.

2.2.3 Type 3: New Dual Mode Sorption Model (NDMS)

In 2007, Feng developed an NDMS with four main assumptions; firstly, the sorption site in a glassy polymer material can be divided into two different species; one is located in the matrix region of the polymer and the other in the microvoids; secondly, all molecules in the matrix region of the polymer have the same partition functions; thirdly, there is GAB sorption in the microvoid region of the polymer; fourthly, the molecules in the layers other than the first layer in the microvoid region have the same partition function as those in the matrix region. Figure 2.3 shows a typical isotherm using new dual mode sorption model. In the NDMS, it was proposed that two modes contribute to water sorption: one corresponds to water in the matrix region of the glassy polymers and follows C_1 which has an upward curve similar to that in rubbery polymers; the other corresponds to water in microvoids and follows C_2 which has a downward trend.The water concentration in the polymer

is given by,

$$C = C_1 + C_2. \tag{2.1}$$

2.2.4 Thermodynamic Models of Water Sorption

Although, some useful insights have been deduced from the application of the discussed empirical models to experimental sorption data, all these models have adjustable parameters. Many groups tried to develop a universal theoretical model capable of predicting the water sorption phenomena in PEMs based on the chemical structure.

One of the most widely used mathematical models is the Flory-Huggins solution theory which explains the thermodynamics of polymer solutions. It calculates an equation for the Gibbs free energy change, ΔG_m, for mixing a polymer with a solvent. Applying the Flory-Huggins theory to the polymer system yields

$$a_w = (1 - \phi_p) \exp[(1 - \frac{1}{r})\phi_p + \chi {\phi_p}^2], \tag{2.2}$$

where a_w is the activity of water, ϕ_p is the volume fraction of polymer, r is the ratio of partial molar volume of polymer membrane $\bar{V}_M$ and solvent $\bar{V}_i$, and χ is The interaction parameter χ was adjusted as a function of activity of water vapour to fit the experimental sorption data of water in vapour phase. However, because the main assumption of Flory-type models is homogeneity in the system, it could not be applied to the systems exhibiting heterogeneity at the micro-scale.

Later on, Muritz *et al.* proposed a sorption model accounting for the equilibrium hydration status of water molecules in Nafion [63]. The main assumption is that the sorption water molecules are confined in the spherical ionic clusters and that all clusters are equivalent chemically and equal in size. The basic thermodynamic formulation is used as before and the swelling pressure was taken as a pressure needed for a spherical hole to stretch its radius from the initial radius r_0 to r in an infinite block of elastic material [63]. However, the main assumption of this model is not correct because they did not take into account the observed dispersion in pore size and the evolution of the pore size distribution in PEM upon water uptake.

More recently, several groups [8, 9, 24, 32, 100] studied the thermodynamics of water uptake considering interfacial energies, elastic energies of polymer walls, as well as entropic effects to explain water uptake of the PEM.

The common problem of the majority of these water sorption models is that they take into account a smaller number of local equilibrium conditions. They only consider equality of chemical potential of the solvent inside of the membrane with that of the solvent outside of the membrane at equilibrium ignoring thermal and mechanical equilibrium. Any models that come up with a smaller number of equilibrium conditions will not be consistent with Gibbs' phase rule. This shortcoming

made them unable to describe the physical state of water as a function of external conditions properly. Some of them assume water vapour inside the PEM further justified by postulating the existence of hydrophobic pores. These assumptions are, however, largely unsupported by experimental data. Data that corroborate hydrophobicity in Nafion channels refer to measurements of wetting angles at external membrane surfaces and are of little validity for microscopic polymer-water interfaces inside PEMs. Moreover, it is observed that the Gibbs free energies of water sorption,ΔG_s are less than Gibbs free energy of vapour sorption at a free water surface at ambient conditions.

Therefore, there is a need for a water sorption model that can explain thermodynamics of water sorption as well as Schroeder's paradox. Eikerling and Berg presented a model of water sorption in PEMs, which could reconcile vapour sorption and porosity data [17]. Details will be discussed in Section 3.1. First step will be to determine the driving force of water sorption in the ionomer which will be discussed in Section 2.3.

2.3 Capillary Effects Dominate Water Sorption in PEM.

The water content, $\lambda = n_{H_2O}/n_{SO_3H}$, is defined as the ratio of the number of moles of water molecules per mol of acid head groups (SO_3H). Water in PEMs is mostly classified into surface and bulk-like water [20, 22, 23],

Surface water creates a much stronger hydrogen-bond interaction with anionic head groups when compared to bulk-like water. Bulk-like water is weakly bonded to anionic head groups and thus exhibits similar conductivity characteristics to bulk water [81].

As discussed, proton conductivity is a strong function of water content. Cappadonia *et al.* explained it by distinction of surface water and bulk-like water. They evaluated conductance of Nafion membranes as a function of temperature and water content [7]. Using an Arrhenius-type analysis of the conductance to calculate the activation free energy of proton conductivity, they observed a dramatic increase of the activation free energy of proton transport from$\sim$ 0.12 eV at $\lambda > 4$ to$\sim$ 0.36 eV at $\lambda < 2$ at high temperature as shown in Figure 2.4.

It is observed that at relatively large water content larger than amount of surface water, $\lambda > \lambda_s$, capillary condensation controls equilibrium water uptake in the membrane. This is supported by comparing the isopiestic vapour sorption of Nafion with pore size distribution data shown in Figures 2.5 and 2.6, respectively. A simple fit function to Figure 2.5 is

$$\lambda = 3.0 \left(\frac{P^v}{P^s}\right)^{0.2} + 11.0 \left(\frac{P^v}{P^s}\right)^4, \tag{2.3}$$

where P^v and P^s are vapour and saturated vapour pressure, respectively. The first term in Equation

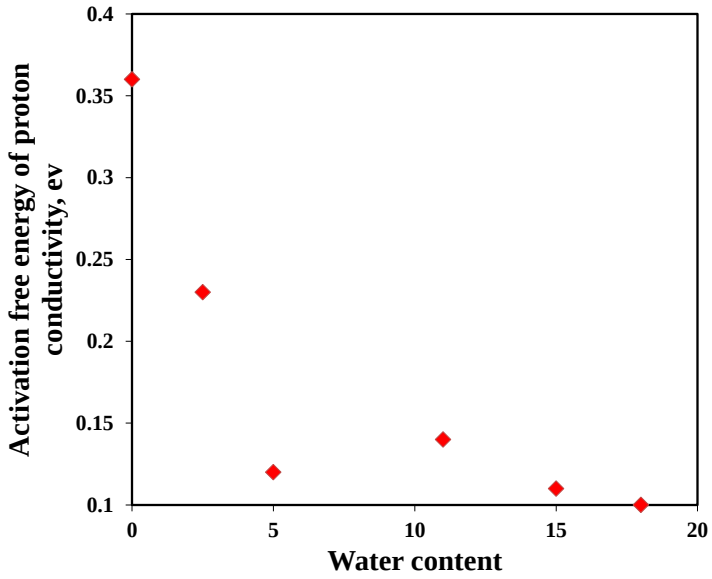

Figure 2.4: Replotted high temperature data of Cappadonia *et al.* [7] on activation free energy of similarly prepared Nafion 117 samples with different water content

2.3 shows a weak dependence on the external vapour pressure and the second term shows a stronger dependence on the external gas pressure. Therefore, the first term can be assigned to surface water near the charged polymer surface and the second term can be identified with bulk-like water.

Figure 2.6 reproduces porosity data [14] with a log-normal pore size distribution, similar to the function suggested in Eikerling et al [22]:

$$\lambda = \frac{\lambda_{max}}{\Lambda} \int_0^{r_c} exp\left(-\left(\frac{\log(r/r_m)}{\log S}\right)^2\right) \mathrm{d}r \tag{2.4}$$

with

$$\Lambda = \int_0^{\infty} exp\left(-\left(\frac{\log(r/r_m)}{\log S}\right)^2\right) \mathrm{d}r, \tag{2.5}$$

where r is the pore radius, r_c the capillary radius, λ_{max} the maximum water content, $r_m = 0.75$ nm and $S = 0.15$. The Gibbs energy of water sorption [78],ΔG_s, can be calculated using

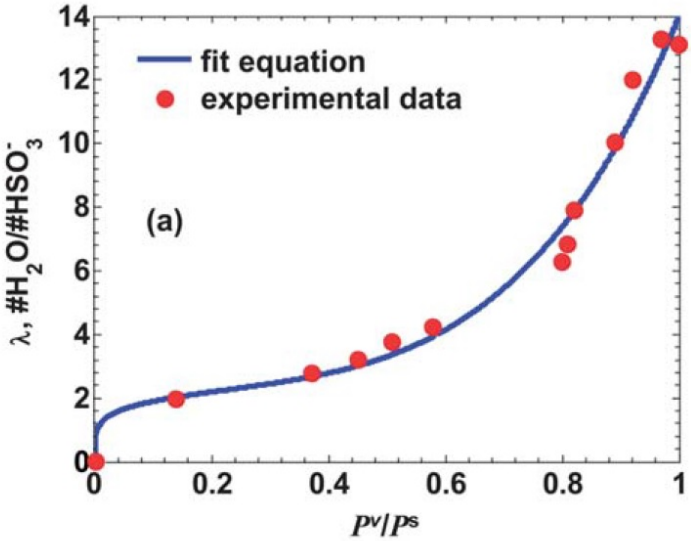

Figure 2.5: Isopiestic water sorption data of Nafion 117 (extracted from [92]) and fit by Equation 2.3 [19].

$$\Delta G_s = \Delta G_w + R_g T \ln \frac{P^v}{P^s}, \tag{2.6}$$

where P^s is the saturated vapour pressure at given T and ΔG_w is the Gibbs free energy of water sorption. The Gibbs free energy of water in pores in the case of capillary condensation is given by

$$\Delta G_c = \Delta G_w - P^c \bar{V_w}, \tag{2.7}$$

where $\bar{V_w}$ is the molar volume of water and the capillary pressure is calculated by

$$P^c = \frac{2\gamma\, cos\theta}{R_c}, \tag{2.8}$$

where γ is the surface tension of water in pores.

Inversion of the experimental relations of water content vs. vapour pressure, $\lambda = f(P^v/P^s)$, as well as vs. capillary radius, $\lambda = g(R_c)$, gives two expressions for the Gibbs free energy of water sorption as functions of λ,

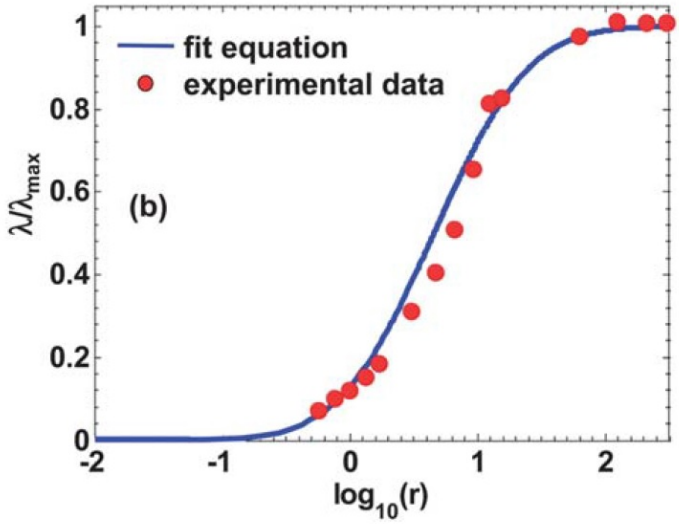

Figure 2.6: Capillary isotherms of Nafion 117 (extracted from ref [14] , r in units of nm) and fit by Equation 2.4 [19].

$$\Delta G_s(\lambda) = \Delta G_w + R_g\, T \ln(f^{-1}(\lambda)) \tag{2.9}$$

and

$$\Delta G_c(\lambda) = \Delta G_w - \frac{2\gamma \bar{V_w}\, cos\theta}{g^{-1}(\lambda)}. \tag{2.10}$$

Comparison of these two expressions obtained from the independent sets of experimental data is shown in Figure 2.7. It shows that at $\lambda/\lambda_{max} > 0.2$ the two graphs are super imposable, which means that $\Delta G_s(\lambda) \approx \Delta G_c(\lambda)$. This supports the idea that in this range capillary condensation is indeed the dominant mechanism of water uptake. The agreement fails for low water content, i.e. at $\lambda < 0.2\lambda_{max}$. At low water content, a significant increase in the strength of water binding is observed. The large energies of water binding at low λ, observed in Figure 2.7, are in agreement with values calculated in *ab initio* quantum mechanical calculations by Roudgar *et al.* [80]

2.4 Challenges for Water Sorption Studies

There are a couple of challenges in order to model of water sorption in PEMS. The main challenge is to establish predictive relations between the chemical structure of the ionomer, membrane structure, and physicochemical properties. Modeling of water sorption in PEMs involves a hierarchy of

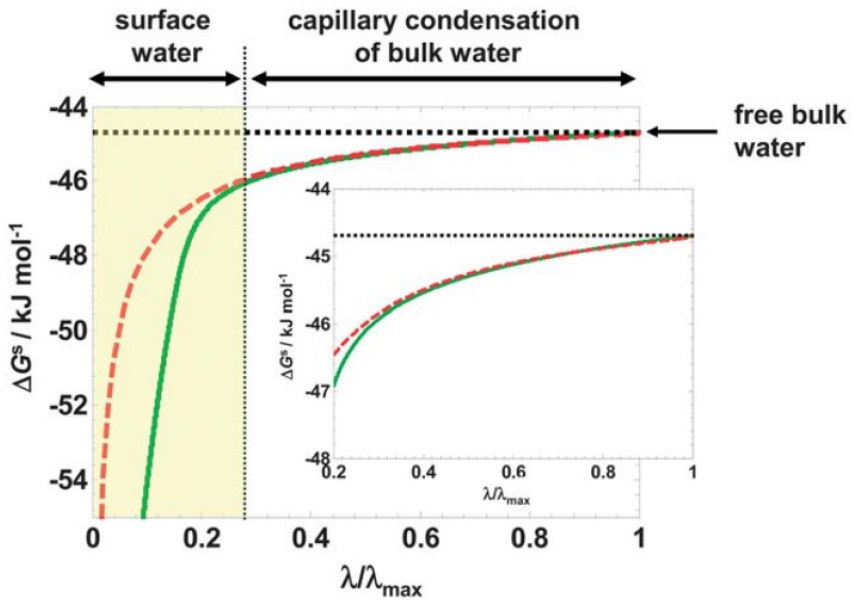

Figure 2.7: Gibbs free energy of water sorption by Nafion 117. Comparison of Gibbs energies obtained from sorption isotherms (green, solid line), corresponding to Figure 2.5, and from capillary isotherms (red, dotted line), corresponding to Figure 2.6 [19].

scales; first, there is self aggregation of polymer rods into bundles of ionomer, then reorganization of the pores and finally macroscopic swelling of the membrane. It is complicated to link microscopic and macroscopic swelling. We need to take into account statistical fluctuations in microscopic membrane properties in order to predict the dispersion in pore sizes and evoultion of pore size distribution upon hydration. We need a predictive model to understand the PEM response to changing external conditions in order to explain and understand Scheröder's paradox.

One of the main challenges in PEFC commercialization is the membrane degradation. Water sorption and swelling models can be a very good diagnostic tool for analysis of degradation. So we need a model which can incorporate the membrane microstructure and its properties.

2.5 Motivation and Objectives

As discussed earlier, most of the physical models had some shortcomings such as applying a single equilibrium condition, assuming the presence of vapour in the membrane, and disagreement with membrane morphological models. Due to the observed viscoelastic properties for PEMs, the membrane cannot be considered as a rigid porous media. At the same time, the membrane cannot be

considered as a solution because of the observed microphase separation of the membrane upon hydration.

In 2011, Eikerling and Berg proposed the poroelectroelastic model of water sorption and swelling of the PEM. In this model they consider the water filled PEM as an charged elastic porous medium. Despite several assumptions and simplifications, this model captures all the relevant physical processes. This model is the basis of this research study.

As discussed in Section 1.4, the membrane is one of the most vulnerable components of a PEFC. Degradation alters the membrane chemical structure, which will affect the internal water and pressure (stress) distribution in the porous network. Changes in water distribution results in change in transport properties and consequently performance of the fuel cell. Internal stresses on the other hand determine the propensity for mechanical degradation. Therefore, water sorption is a key characteristic that links membrane microstructure to transport properties, performance and durability.

The objectives of my work can be summarized as follows :

- Develop a structural based model of water sorption to describe how water uptake and related properties respond to external conditions and structural changes.
- Analyse the impact of degradation on water uptake and structural properties. Moreover, use the multiscale model to describe how nanoscale alterations to the pore shear modulus, morphological rearrangements, and surface charge density could justify the changes in water uptake of the PEM during degradation.

Chapter 3

Theory of Water Sorption and Swelling

3.1 Poroelectroelastic Theory of Water Sorption and Swelling

A recently proposed theoretical model of water sorption and swelling by Eikerling and Berg [17] treats the water-filled PEM as a poroelectroelastic medium with cylindrical pores. The model employs the conditions of thermal, electrochemical, and mechanical equilibrium of water at the pore level. Water uptake and swelling of a single pore is expressed as a function of external conditions and intrinsic materials characteristics of PEMs. The external conditions are defined by temperature, relative humidity and gas pressure. Material properties include ion exchange capacity (IEC), shear modulus of polymer walls and dielectric constant of water in pores.

The model can be applied to pores of various shapes; hereafter, we detail the calculations for cylindrical pores as they are analytically tractable in Section 3.2. In the first step, presented in Section 3.2, the model describes water sorption and swelling at the single pore level. The equilibrium water uptake and swelling by a single pore is determined by T, RH, P^g, as well as elastic properties of pore walls, G, and the interfacial anionic charge density, σ_0. In the second step, discussed in Section 3.4, the model employs convolution of single pore swelling with a statistical distribution of the wall charge density to describe macroscopic swelling in a random ensemble of pores.

3.2 Single Cylindrical Pore Model

Water in the pore is in equilibrium with a surrounding phase at T, P^v, and P^g, as illustrated in Figure 3.1. Corresponding to these thermodynamic variables, equilibrium of water in the pore entails three independent conditions:

- Thermal equilibrium of the ionomer-water system, which implies uniform temperature and zero heat flux in the system.
- Chemical equilibrium, which corresponds to zero water flux and uniform chemical potential of water in the membrane interior and in the external vapour phase,

$$\mu_W^{PEM}(\lambda) = \mu_W^{ext}(a^v) = RT\ln(a^v), \quad a^v = P^v/P^s, \tag{3.1}$$

  where a^v is the activity of external vapour and P^s is the saturated vapour pressure of a free bulk water surface.
- Mechanical equilibrium of water in the pore, which can be expressed as a balance of pressures across all interfaces in the system, involving P^g, P^c, liquid water pressure in the pore, P^l, osmotic pressure, P^{osm}, and elastic pressure exerted by the polymer matrix, P^{el}.

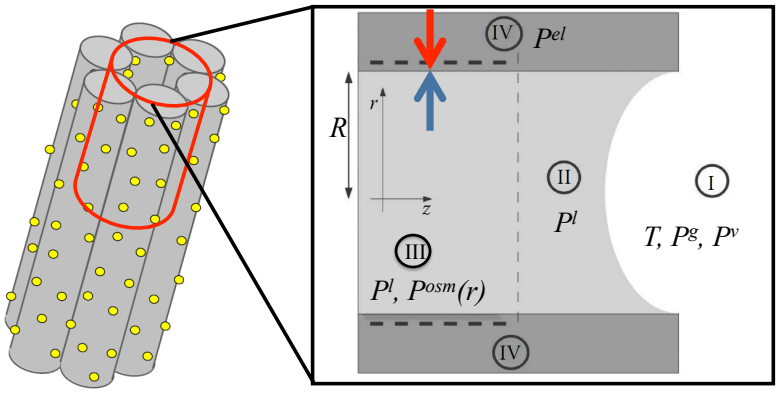

Figure 3.1: Schematic view of a single pore; adopted from [17].

As illustrated in Figure 3.1, four regions have been introduced to describe the process of water sorption at the pore level. For mathematical convenience pores are assumed to be cylindrical with radius R. The surfaces of pores are assumed to be hydrophilic, exhibiting ideal wetting, $\cos\theta = 1$, where θ is the wetting angle. At the single pore level, the dielectric permittivity of water, ϵ_r, is assumed to be constant. The interfacial charge density at pore walls as well as the modulus G of the polymer phase are assumed to be uniform.

Region I is the surrounding phase with given T, P^v, and P^g. Temperature in this region defines the saturation pressure, P^s, and parameters of the polymer-water system including the surface tension of water in pores, γ, the dielectric constant of water in pores, $\varepsilon = \varepsilon_0\ \varepsilon_r$, and the shear modulus of the polymer phase, G. Region II denotes a portion of the nano-pore with uncharged walls, in which the proton concentration is assumed to be zero; P^l determines the state of water in this region. Region III corresponds to the portion of the pore with charged walls, where the distribution of free protons in the pore balances the negative charge at pore walls, representing the anionic surface groups. In this basic version of the model, uniformly charged pore walls are assumed and effects of the discreteness of anionic charges are neglected. In region III, P^l and P^{osm} add up to the total fluid pressure, $P^{fl} = P^l + P^{osm}$, which depends on the separation distance from the pore walls, due to the variation of P^{osm} with proton concentration. Finally, region IV denotes the polymeric phase formed by aggregated ionomer backbones, which experiences a strain as the pore swells, resulting in an elastic pressure, P^{el}.

Two additional constraints are made in order to have the region II:

- A fictitious semipermeable mesh, which is permeable to water molecules and impermeable to protons, must be placed at the interface between regions II and III to keep region II proton-free.
- The elastic constant of polymer walls confining regions II must be adjusted so as to keep the width of the pore uniform.

Due to these constraints, the osmotic pressure vanishes and only the liquid pressure needs to be considered in region II. Local capillary equilibrium of water in pores requires pressures to be balanced at all internal interfaces. The Young-Laplace equation gives the equilibrium pressure difference at the menisci between liquid water in membrane pores and the adjacent phase

$$(P^l)_{II} = (P^g)_I - P^c. \tag{3.2}$$

Equilibrium between regions III and IV can be expressed as a balance of the elastic pressure of the polymer matrix and fluid pressure,

$$(P^{el})_{IV} = (P^{fl})_{III}. \tag{3.3}$$

The liquid pressure is uniform but the total fluid pressure undergoes a discontinuous transition $P^l_{II} \rightarrow P^{fl}_{III}$.

Using Equation 2.8 for capillary pressure and Kelvin-Laplace equation,

$$P^v = P^s exp\left(-\frac{2\gamma \bar{V}_w cos\theta}{R_g T R_c}\right) \tag{3.4}$$

the liquid pressure can be expressed as

$$P^l = P^g + \frac{R_g T}{\bar{V}_w} \ln\left(\frac{P^v}{P^s}\right). \tag{3.5}$$

This equation relates the liquid pressure inside the pore to T, P^v and P^g.

The poroelectroelastic theory of pore swelling relates the charge density, σ_0, at pore walls to a microscopic swelling parameter called η, which is defined as the ratio of the volume of a swollen cylindrical pore to the volume of a unit cell of dry polymer that accommodates a single pore.

The interfacial charge density changes with swelling. This is described by an empirical scaling law,

$$\sigma(R) = \sigma_0 \left(\frac{R_0}{R}\right)^{\alpha}, \tag{3.6}$$

where R_0 is a reference radius (at which σ_0 is defined); the empirical exponent α depends on pore geometry and the extent of surface group reorganization upon swelling. Parameter α represents the degree of surface charge reorganization upon pore swelling. It could take values in the range of $0 < \alpha \leq 2$. A value of α close to 1 represents strong reorganization of anionic surface groups upon swelling. A value of α close to 0 is indicative of weak surface group reorganization. Precise knowledge of α requires microscopic information on self-organization of the hydrated ionomer and structural evolution upon water uptake.

It assumed that the total wall charge is conserved by assuming the conservation of the number of sulfonate anions per pore, $n_{SO^{-3}}$. Therefore, for each pore upon swelling we have

$$n_{SO^{-3}} = \sigma(R) 2\pi R L = \sigma_0 2\pi R_0 L_0. \tag{3.7}$$

Equations 3.7 and 3.6 lead to the following relation between pore radius and length,

$$\frac{R}{R_0}^{\alpha-1} = \frac{L}{L_0}. \tag{3.8}$$

Using the empirical scaling law, the swelling parameter is given by:

$$\eta = \frac{\pi R^2 L}{\nu_0} = \xi \left(\frac{R}{R_0} \right)^{1+\alpha}, \tag{3.9}$$

with

$$\xi = -\frac{R_0 \rho_{SO_3^-}}{2\bar{\sigma_0}}, \tag{3.10}$$

where ν_0 is the volume of a unit cell of dry polymer that contains a single pore, $\rho_{so_3^-}$ is the polymer density and $\bar{\sigma_0}$ is the average wall charge density of the pores.

At capillary equilibrium with an external vapour phase, the liquid pressure can be written as:

$$P^l = P^g - \frac{2\gamma}{R_0} \left(\frac{\xi}{\eta_c} \right)^{\frac{1}{1+\alpha}}, \tag{3.11}$$

where the capillary radius R_c has been expressed in terms of the corresponding swelling parameter, η_c, using Equation 3.9.

The main premise of the model is that local equilibrium of water in pores is described by a balance of pressures across all interfaces. The main condition that determines the state of swelling of a pore is Equation 3.3,

$$P^{el}(\eta) = P^{fl}(\eta) = P^l + P^{osm}(\eta), \tag{3.12}$$

The relation between fluid pressure in pores and proton concentration at equilibrium was derived in Eikerling and Berg [17].

We can start from Stokes equation

$$- \bigtriangledown P - F C_{H^+} \bigtriangledown \phi + \mu \Delta u = 0. \tag{3.13}$$

Since there is no flux because of chemical equilibrium, the velocity is zero, resulting in

$$- \bigtriangledown P - F C_{H^+} \bigtriangledown \phi = 0. \tag{3.14}$$

In order to find $\bigtriangledown\phi$, we can start from Poisson equation,

$$- \bigtriangledown(\varepsilon \bigtriangledown \phi) = \frac{\rho}{4\pi\varepsilon_0}, \tag{3.15}$$

where $\rho = C_+ - C_-$. Since there is no negatively charged species in our system, $\rho = C_{H^+}$. If we assume the constant dielectric to be constant, we get

$$- \bigtriangledown(\bigtriangledown\phi) = \frac{C_{H^+}}{4\pi\varepsilon\varepsilon_0}. \tag{3.16}$$

To obtain an expression for the proton concentration, we employ a Boltzmann distribution,

$$C_{H^+} = C_0 \exp\left(\frac{-F\phi}{RT}\right), \tag{3.17}$$

where C_0 is an integration constant. Substitution into the Equation 3.16 yields the Poisson-Boltzmann equation

$$-\bigtriangledown(\bigtriangledown\phi) = \frac{C_0 \exp\left(\frac{-F\phi}{RT}\right)}{4\pi\varepsilon\varepsilon_0}. \tag{3.18}$$

Using the solution of Poisson- Boltzmann equation replaced in Equation 3.14, the osmotic pressure can be found. After simple math manipulation, the following expression is obtained,

$$P^{osm} = R_g T C_{H^+}(R) = 2\sigma_0 \left[\frac{\sigma_0}{4\varepsilon} - \frac{R_g T}{F R_0}\left(\frac{\xi}{\eta}\right)^{(1-\alpha)/(1+\alpha)}\right]\left(\frac{\xi}{\eta}\right)^{2\alpha/(1+\alpha)}, \tag{3.19}$$

where $C_{H^+}(R)$ is the proton concentration at the pore wall.

Equation 3.12 is the governing equation for the equilibrium of water in a single pore.

Inserting Equations 3.11 and 3.19 into Equation 3.12, the equation of state for equilibrium water uptake by a pore at R_c is obtained,

$$P^{el} = P^g - \frac{2\gamma}{R_0}\left(\frac{\xi}{\eta_c}\right)^{1/1+\alpha} + 2\sigma_0 \left[\frac{\sigma_0}{4\varepsilon} - \frac{R_g T}{F R_0}\left(\frac{\xi}{\eta}\right)^{(1-\alpha)/(1+\alpha)}\right]\left(\frac{\xi}{\eta}\right)^{2\alpha/(1+\alpha)}, \tag{3.20}$$

where we have used η_c to replace R_c, using Equation 3.9.

Solving Equation 3.20 leads to an implicit relation between the wall charge density and the swelling parameter at capillary equilibrium,

$$\sigma_{0,c} = \frac{2\varepsilon R_g T}{F R_0}\left(\frac{\xi}{\eta_c}\right)^{1-\alpha/1+\alpha} \times \left\{1 - \sqrt{1 + \left(\frac{F}{R_g T}\right)^2 \frac{{R_0}^2}{2\varepsilon}\left[P^{el} - P^g + \frac{2\gamma}{R_0}\left(\frac{\xi}{\eta_c}\right)^{1/1+\alpha}\right]\left(\frac{\xi}{\eta_c}\right)^{-2/(1+\alpha)}}\right\}. \tag{3.21}$$

Equation 3.21 describes the water uptake of a single pore in equilibrium with a surrounding gas phase at total pressure P^g and T. The value of η_c can be related to relative humidity Equations 3.4 Equation 3.21 establishes the relation between environmental conditions (T, P^v, P^g) and the swelling parameter, η_c. Pressure equilibrium in a single pore is illustrated in Figure 3.2. At each

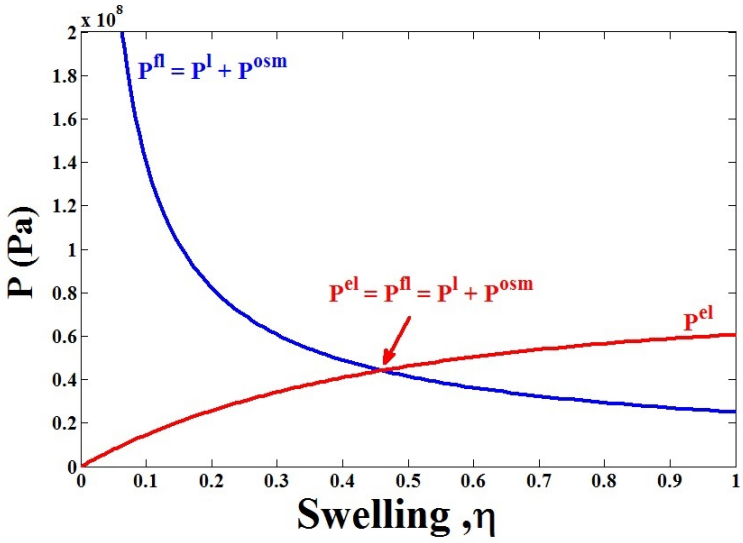

Figure 3.2: Pressure equilibrium between fluid pressure, P^{fl}, and elastic pressure, P^{el}, at the pore wall for a certain σ_0 value.

value of σ_0, can be solved to obtain an equilibrium swelling parameter, η. When RH is increasing, if the pore has the right value of σ_0, it will swell to an equilibrium radius, R_c. During swelling, the fluid pressure decreased due to decrease in osmotic pressure, while the elastic pressure increases. Pressure balance is reached at a point for each value of σ_0, shown in Figure 3.2.

In terms of materials properties, the water uptake depends on the local wall charge density, dielectric properties of water, and elastic properties of polymeric pore walls. If the surface charge density of the pore increases, the pore needs a higher value of the RH in order to start filling. The reason is that swelling requires a sufficient osmotic pressure, which increases with σ_0. Larger osmotice pressure forces the pore to swell to a larger swelling parameter and consequently larger radii, as shown in Figure 3.3. This figure illustrates that different values of σ_0 corresponds to different values of η.

A similar relation between wall charge density and swelling parameter is obtained for the liquid-equilibrated case, when water in the pore is in equilibrium with an external bulk water phase at the liquid pressure, P^l_{ext},

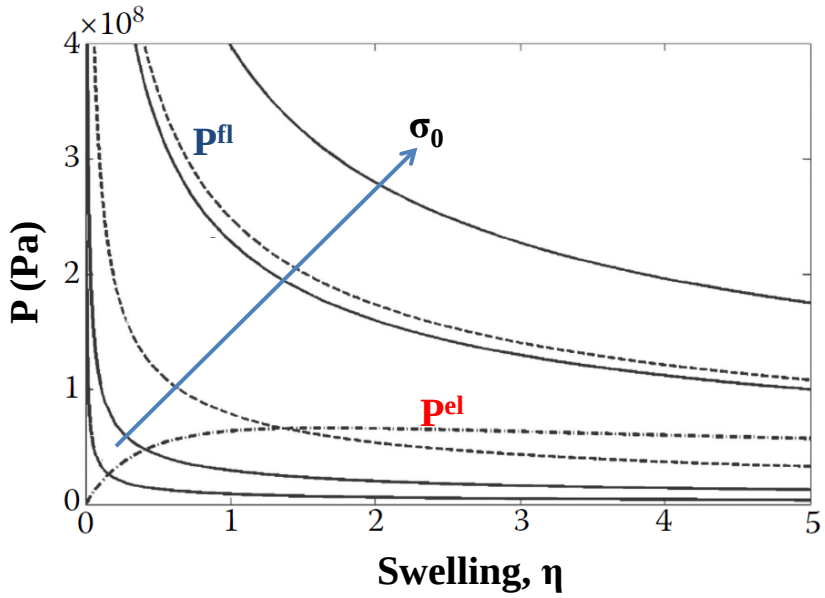

Figure 3.3: effect of increase in value of σ_0 on swelling of the single pore.

$$\sigma_{0,c} = \frac{2\varepsilon R_g T}{F R_0} \left(\frac{\xi}{\eta}\right)^{1-\alpha/1+\alpha} \times \left\{1 - \sqrt{1 + \left(\frac{F}{R_g T}\right)^2 \frac{{R_0}^2}{2\varepsilon} \left[P^{el} - {P^l}_{ext}\right] \left(\frac{\xi}{\eta}\right)^{-2/(1+\alpha)}}\right\}. \quad (3.22)$$

In Equations 3.21 and 3.22 the elastic pressure, P^{el}, has been left unspecified. In Ref. [17], the authors considered a scenario for the deformation of polymer walls that was based on Freger's approach [28]. In section 3.3, we will discuss alternative deformation scenarios derived in this work.

To summarise this section, water sorption at the pore level involves three steps. First, at insufficient relative humidity, a pore does not contain any bulk-like water so it is in a collapsed state. Once a critical relative humidity is reached, determined by wall charge density of the pore, the pore discontinuously fills with water up to an equilibrium swelling level, described by Equation 3.21. When saturated vapour is replaced by liquid water, pores undergo a discontinuous swelling transition to a larger swelling parameter η_l, given by Equation 3.22, and thus to a larger equilibrium radius.

3.3 Stress-Strain Relationships of Microscopic Pore Walls

Most models of swelling phenomena in polymer materials utilize the statistical theory of rubber elasticity to establish a relation between swelling pressure and η_c. One of the earliest models, developed by Flory [27], assumes random mixing of solvent and monomers; it uses the Bragg-Williams approximation to account for interactions between different components [48]. Moreover, it considers a mechanism of affine swelling, in which there is no structural reorganization at the molecular scale and junction points between polymer chains are shifted proportionally to the macroscopic swelling deformation. Following this assumption, the change in the free energy due to the elastic deformation of the swollen polymer, F^{el}, can be calculated for a given representation of the polymer chain length distribution.

Several models relate P^{el} to η_c based on the assumption of affine swelling [46, 70, 84, 108]. The Flory-Rehner theory considers an affinely deformed network of N walls. For such a system, the following expression for the free energy of deformation per unit volume can be derived,

$$F^{el} = \frac{1}{2} G \sum_{ij} \left(c \, \ln \beta_{ij} + {\beta_{ij}}^2 - 1 \right) \tag{3.23}$$

where the summation is over the walls and the microscopic axes, $G = \frac{NKT}{V_0}$ is the shear modulus and V_0 is the volume of the dry polymer. The value of the parameter c should be in the range of 0 to 1 [26]. However, this parameter is of no relevance in our free energy calculations because the logarithmic term cancels out. β_{ij} are components of the deformation tensor, $\bar{\bar{\beta}}$, which is defined as

$$\bar{\bar{\beta}} = \begin{pmatrix} \beta_{x,x} & \beta_{x,y} & \beta_{x,z} \\ \beta_{y,x} & \beta_{y,y} & \beta_{y,z} \\ \beta_{z,x} & \beta_{z,y} & \beta_{z,z} \end{pmatrix} \tag{3.24}$$

The stress is applied normal to the surface of the wall and we assume that wall deformation involves neither twisting nor torsion. Therefore, the deformation tensor can be written as

$$\bar{\bar{\beta}} = \begin{pmatrix} \beta_{x,x} & 0 & 0 \\ 0 & \beta_{y,y} & 0 \\ 0 & 0 & \beta_{z,z} \end{pmatrix}.$$

However, the assumption of affine swelling is not valid when macroscopically homogeneous swelling is accompanied by phase separation at the microscale. It has been observed that PFSA ionomer membranes exhibit non-affine swelling, i.e. there is structural reorganization, in which the strain experienced by microscopic pore walls is significantly higher than the overall macroscopic swelling strain [56]. Models that are based on the classical theory of rubber elasticity cannot be used to determine the swelling pressure in structures with non-affine swelling behavior.

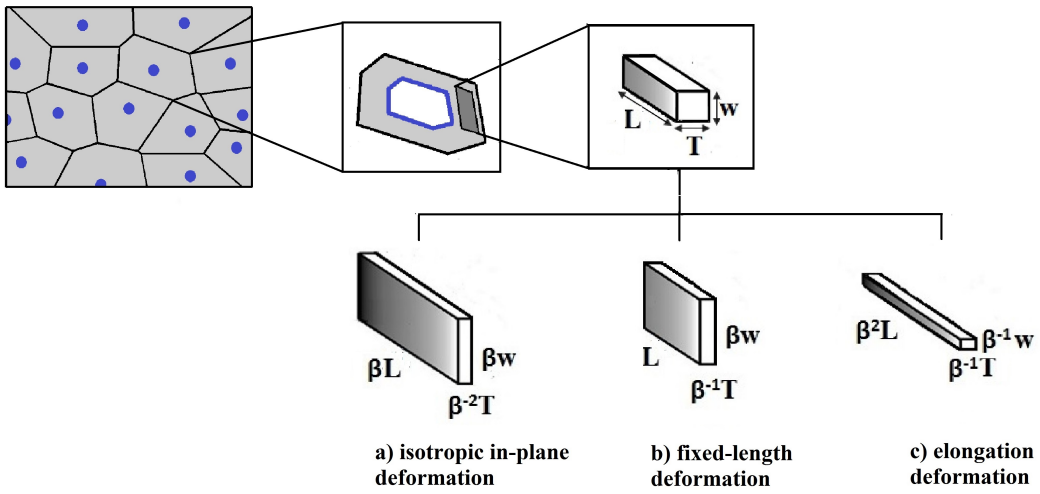

Figure 3.4: The top panel shows a schematic cross-section of the membrane represented by a Voronoi tessellation, adopted from Ref. [28]. Zoomed in picture shows a single cell with pore walls (gray) and a swollen core (middle) as well as a single wall element (right). The bottom panel shows the three swelling scenarios considered in this work, corresponding to (a) in-plane isotropic deformation; (b) fixed-length deformation; (c) elongation of wall-forming elements.

A study that accounted for the non-affine swelling of PFSA was conducted by Freger [28]. Freger developed an expression for the free energy of a polymer swollen in water by assuming a volume-conserving deformation of each wall in the Flory-Rehner model [27]. The model of Freger represents the swollen polymer matrix as a Voronoi tessellation; each polyhedral cell encapsulates a water droplet as shown in Figure 3.4. Upon swelling, walls of each cell undergo compression in thickness direction. We evaluate three scenarios for the deformation of polymer walls illustrated in Figure 3.4. (A) isotropic in-plane deformation, (B) fixed-length deformation, and (C) elongation of wall-forming elements. For isotropic in-plane deformation walls expand equally in both transverse directions. For fixed-length deformation, the length of the pore is conserved and polymer walls expand in width direction only. In the third scenario, we consider elongation of polymer elements that form pore walls (bundles, fibrils, ribbons). Since the volume of the polymer phase is conserved during swelling, the product of the three deformation ratios along the three spatial directions in the deformation tensor has to be one. The deformation tensors can thus be written as

$$\bar{\bar{\beta}}_A = \begin{pmatrix} \beta^{-2} & 0 & 0 \\ 0 & \beta & 0 \\ 0 & 0 & \beta \end{pmatrix}, \quad \bar{\bar{\beta}}_B = \begin{pmatrix} \beta^{-1} & 0 & 0 \\ 0 & \beta & 0 \\ 0 & 0 & 1 \end{pmatrix} \quad \text{and} \quad \bar{\bar{\beta}}_C = \begin{pmatrix} \beta^{-1} & 0 & 0 \\ 0 & \beta^{-1} & 0 \\ 0 & 0 & \beta^2 \end{pmatrix}, \tag{3.25}$$

for the cases of isotropic, fixed-length and elongation deformation, respectively. We use an empirical relation to express β as a function of the polymer volume fraction,

$$\beta = \phi_p^{-\frac{1}{3}}, \tag{3.26}$$

where ϕ_p is the polymer volume fraction, defined as the ratio of the volume of the non-swollen network, V_0, to the total volume, $\phi_p = \frac{1}{\eta+1}$

By summation over the principal axes of the film, we derive the free energy of deformation, using Equation (3.23), for three different scenarios, following the formalism proposed in Ref. [28],

$$F^{el}{}_A = \frac{1}{2} G \left(2\,\beta^2 + \beta^{-4}\right), \tag{3.27}$$

$$F^{el}{}_B = \frac{1}{2} G \left(\beta^2 + \beta^{-2}\right), \tag{3.28}$$

and

$$F^{el}{}_C = \frac{1}{2} G \left(\beta^4 + 2\beta^{-2}\right). \tag{3.29}$$

Using Equation (3.26), free energies of deformation can be written as

$$F^{el}{}_A = \frac{1}{2} G \left(2\,{\phi_p}^{-2/3} + {\phi_p}^{4/3}\right), \tag{3.30}$$

$$F^{el}{}_B = \frac{1}{2} G \left({\phi_p}^{-2/3} + {\phi_p}^{2/3}\right), \tag{3.31}$$

and

$$F^{el}{}_C = \frac{1}{2} G \left({\phi_p}^{-4/3} + 2{\phi_p}^{2/3}\right). \tag{3.32}$$

The change of the free energy at constant temperature and number of molecules is

$$dF = -P\,dV. \tag{3.33}$$

The elastic pressure is obtained from

$$P^{el} = -\frac{\partial F^{el}}{\partial V} = -\frac{{\phi_p}^2}{V_0}\frac{\partial F^{el}}{\partial \phi_p}. \tag{3.34}$$

Differentiating Equations (3.30), (3.31) and (3.32) hence gives

$$P^{el}{}_A = \frac{2}{3}G\left({\phi_p}^{\frac{1}{3}} - {\phi_p}^{\frac{7}{3}}\right) = \frac{2}{3}G\left(\left(\frac{1}{\eta_c+1}\right)^{\frac{1}{3}} - \left(\frac{1}{\eta_c+1}\right)^{\frac{7}{3}}\right), \tag{3.35}$$

$$P^{el}{}_B = \frac{1}{3}G\left({\phi_p}^{\frac{1}{3}} - {\phi_p}^{\frac{5}{3}}\right) = \frac{1}{3}G\left(\left(\frac{1}{\eta_c+1}\right)^{\frac{1}{3}} - \left(\frac{1}{\eta_c+1}\right)^{\frac{5}{3}}\right) \tag{3.36}$$

and

$$P^{el}{}_C = \frac{2}{3}G\left({\phi_p}^{-\frac{1}{3}} - {\phi_p}^{\frac{5}{3}}\right) = \frac{2}{3}G\left(\left(\frac{1}{\eta_c+1}\right)^{-\frac{1}{3}} - \left(\frac{1}{\eta_c+1}\right)^{\frac{5}{3}}\right), \tag{3.37}$$

where the relation $\phi_p = \frac{1}{\eta_c+1}$ was used to relate the elastic pressure to the microscopic swelling parameter defined in Equation 3.9.

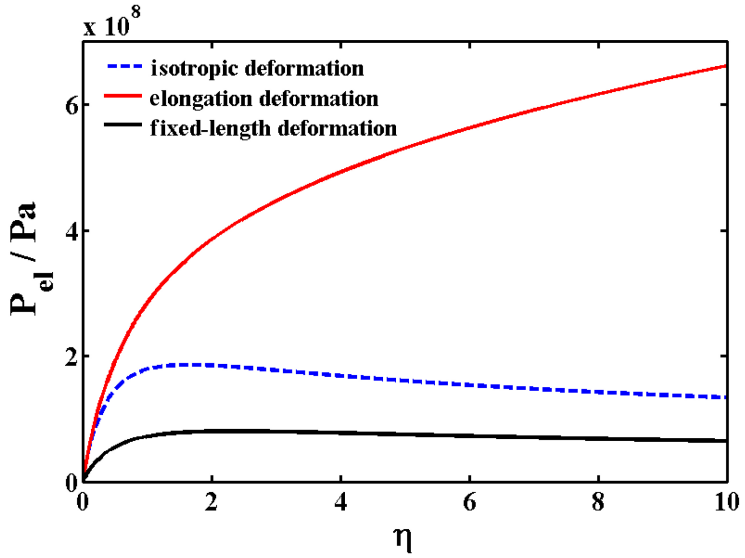

Figure 3.5: Elastic pressure for the different deformation scenarios illustrated in Figure 3.4 as a function of the swelling parameter η.

The elastic pressure in Equations (3.35), (3.36) and (3.37) approaches zero under dry conditions, as expected, and it rises linearly for low degree of swelling. At higher degree of swelling, P^{el} goes through maximum and then decreases in case of isotropic deformation. Figure 3.5 illustrates the elastic pressure as a function of η_c for the three different scenarios. In Section 3.4, we evaluate these deformation scenarios by comparison with experimental data.

3.4 Pore Ensemble Model

SAXS, SANS, porosimetry, and water sorption studies of PEMs show a dispersion in pore sizes and an evolution of the pore size distribution during water uptake. Eikerling and Berg related the dispersion in pore sizes to fluctuations in the surface charge density in the reference state, σ_0. The total water sorption of the membrane is obtained by summing up elementary contributions from each unit cell. Mathematically this corresponds to a convolution of the single pore swelling parameter with the statistical pore density distribution, given as a function of wall charge density in the reference state, n(σ_0).

The volumetric expansion upon swelling is

$$\frac{\Delta V}{V_0} = \frac{1}{N_{uc}} \int_0^{{\sigma_0}^{max}} n(\sigma_0)\, \eta(\sigma_0, \sigma_{0,c})\, \mathrm{d}\sigma_0 \tag{3.38}$$

with the function $\eta(\sigma_0, \sigma_{0,c})$ obtained from Equation 3.21.

The parameterN_{uc} in Equation (3.38) is a normalization factor

$$N_{uc} = \frac{V_0}{\nu_0} = \int_0^{{\sigma_0}^{max}} n(\sigma_0)\, \mathrm{d}\sigma_0. \tag{3.39}$$

Knowledge of the statistical pore density distribution as a function of surface charge density, n(σ_0), is a requirement to predict the water sorption behaviour of a PEM. However, we cannot determine it from existing experimental data. If we assume a monodisperse distribution function n(σ_0), we will not get the sigmoid shape sorption isotherm because at a certain RH, all pores start to fill. If RH increases, P^l increases as well and causes further swelling of pores. The sorption behaviour of a mono-dispersed system is illustrated schematically in Figure 3.6.

We will thus assume to have the following general requirements: 1) it is a continuous distribution, 2) its integral is consistent with the ion exchange capacity, which is defined as the number of moles of sulfonic acid groups per gram of dry polymer and 3) it has a single peak. We evaluated different functional forms of the probability distribution $n(\sigma_0)$, namely Gaussian and log-normal functions, as shown in Figure 3.7.

The maximal wall charge density ${\sigma_0}^{max}$ can be determined from *ab initio* simulations of arrays of charged surface groups [80]. Calculations suggest a maximal density of sulfonic head groups of ${\sigma_0}^{max} = -0.52$ C m^{-2}. For $\sigma_0 > {\sigma_0}^{max}$, water molecules and hydronium ions would be squeezed out from the space between anionic head groups and strong electrostatic interactions between anions would destabilize the polymer matrix. σ_0^{max} is thus the cut-off charge density of the distribution.

To validate the model, it is essential to compare it with experimental water sorption data. For this purpose, we have to relate the volumetric expansion to the water content, λ. Water content

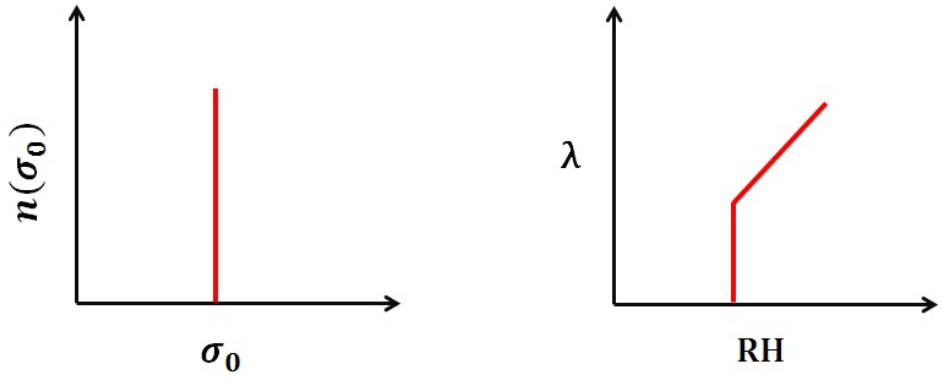

Figure 3.6: Schematic sorption behaviour of an ensemble of pores with monodispersed function n(σ_0).

is normally defined as the number of water molecules per anionic head group. The volumetric expansion of the PEM, normalized to the dry PEM volume, is related to λ via the following relation,

$$\left(\frac{\Delta V}{V_0}\right) = IEC\rho_p\bar{V}_w\lambda, \tag{3.40}$$

where $\bar{V}_w$ is molar volumes of water and ρ_p is polymer density. The volume change due to water uptake can be obtained from

$$\frac{\Delta V}{V_0} = \frac{1}{N_{uc}}\int_0^{\eta_c} \mathrm{d}\eta\; n(\sigma_0)\;\eta\;\frac{\mathrm{d}\sigma_0}{\mathrm{d}\eta}. \tag{3.41}$$

Water uptake in PEM involves three processes, corresponding to pore filling, continuous pore swelling and a discontinuous swelling transition upon replacing a vapour atmosphere by a liquid water bath. Pore filling denotes the discontinuous process described in Section 3.2, by which an initially dry pore attains its capillary radius R_c in equilibrium with water vapour, determined by the Kelvin-Laplace equation. With increasing RH, capillary equilibrium advances to pores with larger R_c and thus larger swelling parameter η_c. Equation 3.21 determines the corresponding value of $\sigma_{0,c}$. The liquid pressure, given by Equation 3.11, increases as well with $\sigma_{0,c}$. Pressure equilibrium demands that the liquid pressure, established in the critical pores at $\sigma_{0,c}$, is homogeneous and isotropic. Thus, the same liquid pressure applies in all pores with $\sigma_0 < \sigma_{0,c}$ that have been already filled with water. Due to the increase in P^l, these pores will undergo continuous swelling to attain new equilibrium values of η. Maximal swelling of a PEM in a vapour atmosphere is reached when $\sigma_{0,c} = {\sigma_0}^{max}$.

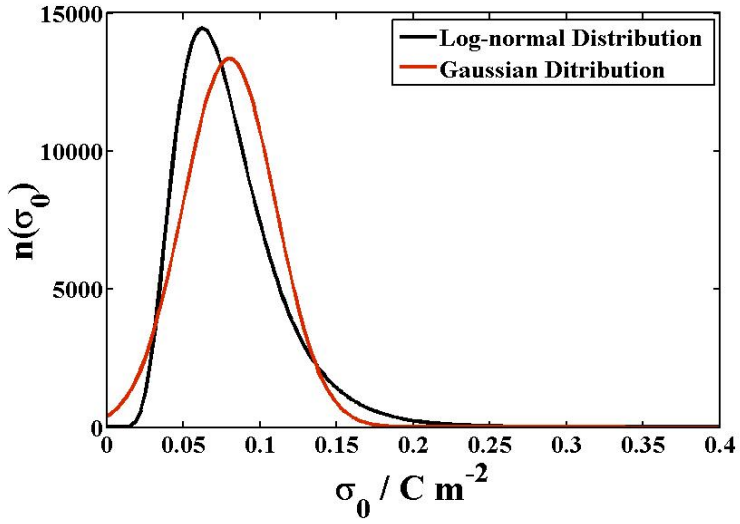

Figure 3.7: Surface charge density distribution of an ensemble of pores: the black line shows a log-normal distribution function and the red line shows a Gaussian distribution of surface charges.

If saturated vapour is replaced by liquid water, the membrane will swell more. Upon this transition, the liquid pressure changes discontinuously from $p^{l,max} = p^g - \left(\frac{2\gamma}{R_0}\right)\left(\frac{\xi}{\eta_c{}^{max}}\right)^{1/1+\alpha}$ in saturated vapour to $P^l = P^g$ in liquid water. Mostly, this discontinuity in water uptake is referred to as so-called Schreöder's paradox. This discontinuity in the fluid pressure in pores explains the apparent paradox as a first-order phase transition. In case of liquid equilibrated membrane, there will be higher liquid pressure to open the pores and that's one reason that the membrane could uptake more water that vapour equilibrated case. The magnitude of this jump, which is larger in experiment most of the time, depends on n(σ_0) and is sensitive to values of α, σ_0, G, IEC and T.

3.5 Calculation of Pore Volume Distribution

Here, we describe how to calculate the differential pore volume distribution, which is defined as the relation between $\frac{\mathrm{d}}{\mathrm{d}R}(\frac{\Delta V}{V_0})$ and R. The total volume change due to water uptake can be calculated from Equation 3.38, which we can rewrite as a function of the swelling parameter as follows,

$$\frac{\Delta V}{V_0} = \frac{1}{N_{uc}} \int_0^{\eta_c} \mathrm{d}\eta \; n(\sigma_0) \; \eta \; \frac{\mathrm{d}\sigma_0}{\mathrm{d}\eta}. \tag{3.42}$$

Using the above equation, we get the following equation for $\frac{\mathrm{d}}{\mathrm{d}R}(\frac{\Delta V}{V_0})$,

$$\frac{\mathrm{d}}{\mathrm{d}R}\left(\frac{\Delta V}{V_0}\right) = \frac{1}{N_{uc}}\left(n(\sigma_0)\ \frac{(1+\alpha)\xi^2}{R_0}\ \left(\frac{R}{R_0}\right)^{1+2\alpha}\ \frac{\mathrm{d}\sigma_0}{\mathrm{d}\eta}\right). \tag{3.43}$$

The integration variable is the swelling parameter, η, which is defined as

$$\eta = \xi(\frac{R}{R_0})^{1+\alpha}. \tag{3.44}$$

Therefore, the derivative with respect to η yields

$$\frac{\mathrm{d}}{\mathrm{d}\eta}(\frac{\Delta V}{V_0}) = \frac{\mathrm{d}}{\mathrm{d}\eta}\left(\frac{1}{N_{uc}}\int_0^{\eta_c}\mathrm{d}\eta n(\sigma_0)\eta\frac{\mathrm{d}\sigma_0}{\mathrm{d}\eta}\right) = \frac{1}{N_{uc}}\times\left(n(\sigma_0)\eta\frac{\mathrm{d}\sigma_0}{\mathrm{d}\eta}\right). \tag{3.45}$$

Using the chain rule of differentiation, we find an expression for the differential pore volume distribution function of the form

$$\frac{\mathrm{d}}{\mathrm{d}R}\left(\frac{\Delta V}{V_0}\right) = \frac{1}{N_{uc}}\left(n(\sigma_0)\ \eta\ \frac{\mathrm{d}\sigma_0}{\mathrm{d}R}\right), \tag{3.46}$$

which implies that

$$\frac{\mathrm{d}\sigma_0}{\mathrm{d}R} = \left(\frac{(1+\alpha)\xi^2}{\eta\ R_0}\ \left(\frac{R}{R_0}\right)^{1+2\alpha}\ \frac{\mathrm{d}\sigma_0}{\mathrm{d}\eta}\right). \tag{3.47}$$

Figure 3.8b shows the differential pore volume distribution obtained using a Gaussian and log-normal distribution function for $n(\sigma_0)$. Parameters are given in Table 3.1. As is obvious in Figure 3.8b, the two curves differ in the tail region at large values of the pore radius. Comparison of these calculated pore volume distributions with experimental data as well as modeling work [20] reveals that the log-normal distribution yields better agreement with experiment.

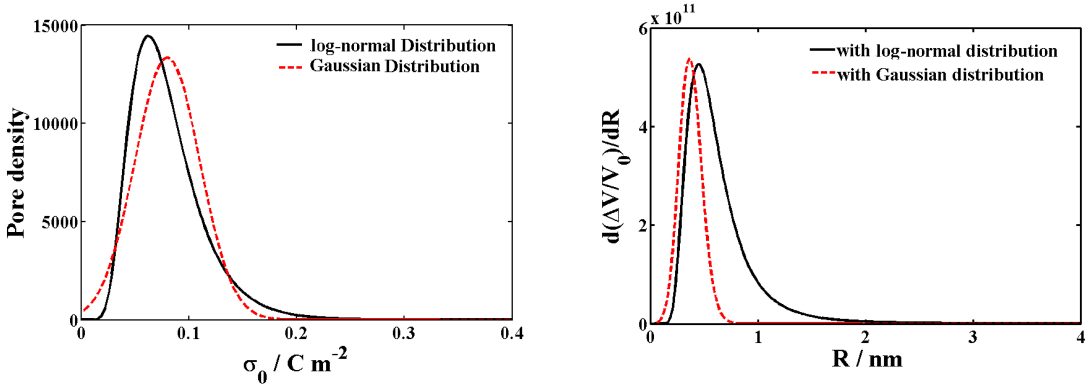

(a) (b)

Figure 3.8: (a) Statistical pore density distribution vs. surface charge density of an ensemble of pores. The red dashed line shows a Gaussian distribution function and the black solid line a log-normal distribution function. (b) Differential pore volume as a function of pore radius for different pore density distributions in (a).

Reference set of parameters	Symbol	Value	Unit
Temperature	T	298	K
Gas Pressure	P^g	0.1	MPa
Ion Exchange Capacity	IEC	0.91	mol/kg
Density of dry polymer	ρ_p	2000	kgm^{-3}
Reference Radius	R_0	1	nm
Surface Tension of water	γ	0.072	N m^{-1}
Contact Angle	θ	0	-
Mean wall charge density	$\bar{\sigma_0}$	-0.08	Cm^{-2}
Dielectric Permittivity	ε_r	25	-
Standard deviation in wall charge density distribution	d_σ	0.034	Cm^{-2}
Degree of surface charge reorganization	α	0.5	-
Shear modulus	G	0.38	GPa

Table 3.1: Reference set of parameters

Chapter 4

Results and Discussion

4.1 Parametric studies and Experimental Comparison

The main input function of the water sorption model is the distribution function, $n(\sigma_0)$, which must be given for a reference state. We use a log-normal distribution because it yields a more consistent in terms of pore volume distribution of the pores, as discussed at the end of last section.

Other material-specific parameters that must be given to study the water sorption properties of a PEM are the IEC, the shear modulus, G, the dielectric constant of water in the pores, ε_r, and the parameter representing the reorganization of surface charges, α. Parameters are provided in Table 3.1. In the list of parameters, we have good understanding of the first seven parameters. Temperature and gas pressure are externally controlled. The IEC and ρ_p have been measured in the experiments that we have analysed. The reference radius was chosen deliberately as $R_0 =$ 1 nm. The surface tension of water, γ, is an experimentally well-measured quantity. For water in pores, we assume perfect wetting, thus cos $\theta = 1$. We calculated the mean wall charge density in the reference state, $\bar{\sigma_0}$, from the structural characteristics of Nafion (grafting density and aggregation [64]); this approach yields $\bar{\sigma_0} = 0.08$ C m^{-2} for membranes with an IEC of about 0.9 mmol g^{-1}. For the dielectric permittivity, ε_r, modeling studies suggest a value in the range of 10-15 in the surface water layer at pore walls and 80 for bulk-like water in the pore centre [72]. We have used an effective dielectric permittivity $\varepsilon_r = 25$ for water. With this information and comparing model isotherms with experimental data, we found that the standard deviation, d_{σ_0}, which will give us best agreement, is 0.034 C m^{-2} for fresh membranes. A value of 0.5 was used for α. Therefore, G was left over as the only free parameter that we determined from the analysis of water sorption data for a fresh membrane. We used R-square as a statistical measure to evaluate the goodness of our fits.

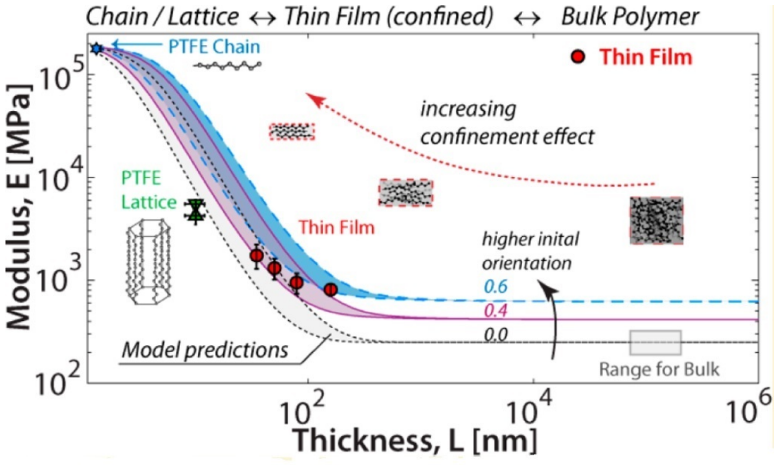

Figure 4.1: Shear modulus of Nafion as a function of film thickness [71].

Experimental values of the shear modulus for Nafion range from 160-200 MPa [42]. These values represent an effective macroscopic shear modulus. The input of the model is however the microscopic shear modulus for polymer bundles or walls that confine pores. Exact experimental values for this microscopic property are not available. It is reasonable to expect that the microscopic shear modulus at the pore level is significantly larger than its macroscopic counterpart, which is a volume-averaged parameter [87]. In agreement with this inference, an increase in shear modulus has been observed in ionomer thin-film systems compared to ionomer with larger thickness, studied experimentally in Ref. [71]. As illustrated in Figure 4.1, when Nafion is confined to thin films, there is a drastic increase in the shear modulus over the bulk value and the mechanical response becomes dominated by the modulus of individual polymer chains.

Sorption isotherms have been calculated for the three deformation scenarios discussed in Section 3.3, namely the isotropic deformation, fixed-length deformation, and axial stretching scenario. The results are compared with two sets of experimental data in Figure 4.2 [61, 106]. Experimental data have been corrected by subtracting the amount of surface water from the total water content. The fixed-length deformation scenario gives the best agreement with water sorption data, if a realistic value of the microscopic shear modulus, G, consistent with microscopic elastic properties of Nafion, is used. A rationalization of this finding at the microstructure level is beyond the scope of our work. It will require detailed molecular level simulations, which we are currently performing in our group.

A sensitivity analysis with respect to the key parameters, viz. ε_r, d_σ, α, and G, was conducted; for a meaningful analysis, we evaluated the parameter variation necessary to bring about a change

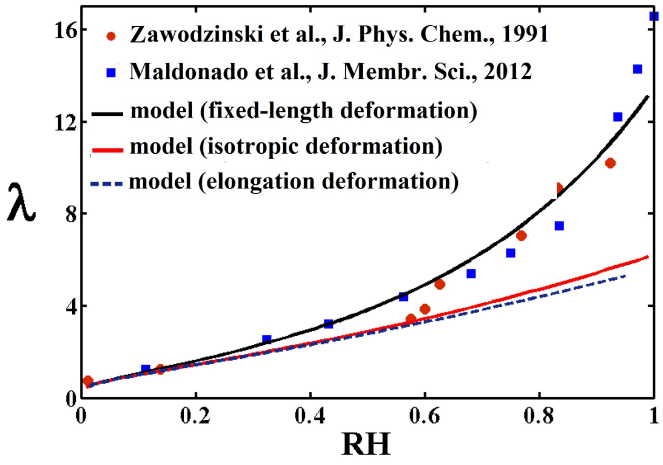

Figure 4.2: Sorption isotherm calculated using the fixed-length deformation (black line), isotropic in-plane deformation (red line) and elongation (blue dashed line) scenarios, defined in Figure 3.4, of polymer walls in comparison with two sets of experimental data [61, 106].

in water sorption by +/- 5% at 90% RH. The analysis revealed a high sensitivity to the ε_r (8% variation required) and G (10% variation required), and a lower sensitivity to d_σ (30% variation required) and α (25% variation required). It is worthy of note that experimental studies also exhibit significant uncertainty because of the dependency of water sorption data to pre-treatment procedures, as can be seen in Figure 4.2.

Swelling of the PEM is sensitive to the parameter α, as shown in Figure 4.3. For $\alpha = 1$, the polymer swells more because of strong reorganization of the surface charges. In order to have finite-size pores, it is necessary to have $\alpha > 0$. A value of α = 0.5 was considered in Ref. [17] to represent the case of cylindrical pores.

4.1.1 Alcohol Sorption

In addition to water sorption, the poroelectroelastic model can be used to calculate alcohol sorption. We calculated the volumetric expansion of Nafion in methanol and ethanol and compared them with available experimental data [107]. Figure 4.4 shows good agreement of the model with these data. Sets of parameters used for calculations are listed in Table. 4.1. The volumetric expansion of the PEM is largest in ethanol followed by methanol and water. These trends can be rationalized with

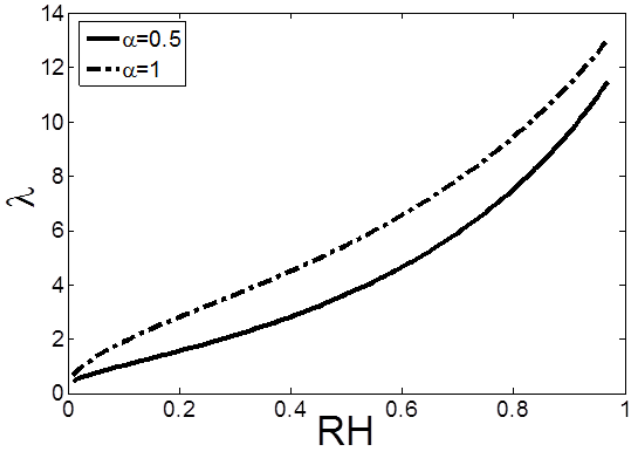

Figure 4.3: Effect of degree of surface charge reorganization on sorption behaviour of the PEM.

the identified changes in ε_r and G. As ε_r decreases, the osmotic pressure that swells pores is bound to increase. Moreover, the less polar solvents result in weaker phase separation, softening the polymer matrix and leading to a reduction of G. The net effect is a larger volumetric expansion. For the purpose of displaying this effect, experimental data for λ have been converted to $\frac{\Delta V}{V_0}$, using the linear relation in Equation 3.40. To achieve good agreement with experimental data, we had to use a lower degree of surface charge reorganization, represented by α, and a larger $\bar{\sigma_0}$ for swelling in ethanol and methanol. These findings suggest that more pronounced structural changes occur when water is exchanged for ethanol and methanol.

	Water	**Methanol**	**Ethanol**	**Unit**
Shear modulus (G)	380	230	205	MPa
Dielectric constant (ϵ_r)	25	13	10	-
Molecular weight	18.01	32.04	46.07	g mol^{-1}
Reorganization parameter (α)	0.5	0.2	0.2	-
Average wall charge density ($\bar{\sigma_0}$)	0.08	0.15	0.21	C m^{-2}
Surface tension (γ)	0.072	0.022	0.022	N m^{-1}
Molar volume ($\bar{V}$)	18.06 $\times$ 10^{-6}	40.50 $\times$ 10^{-6}	58.30 $\times$ 10^{-6}	m^3

Table 4.1: Sets of parameters for sorption isotherms in Figure 4.4.

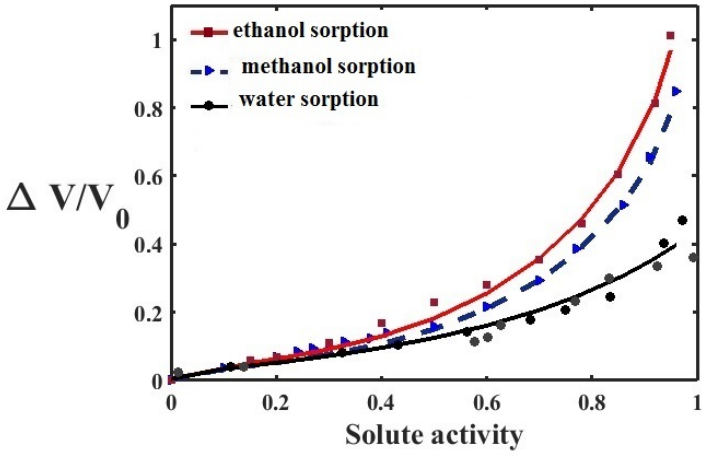

Figure 4.4: Volumetric expansion of Nafion 1100 in water, methanol and ethanol.

4.1.2 Impact of External Conditions

As shown in Figure 4.5, varying gas pressure has low impact on water sorption. Water sorption is rather insensitive to an increase in P^g. This behaviour was observed in experiments before. The reason is that $P^g \ll P^{osm}$, P^{el}, P^c. Gas pressure is normally two or three orders of magnitude smaller than P^{el}, P^c and P^{osm} but small variations in $\frac{P^v}{P^s}$ cause large variations in internal liquid pressures in pores, establishing substantial driving forces for hydraulic water fluxes [14, 22].

Temperature could have a larger and more complex impact because dielectric constant, ε_r, shear modulus, G, and surface tension, γ are functions of temperature. The effect of T could be ambiguous resulting from different pressure contributions that depend on it. In Figure 4.5, water sorption of Nafion is calculated at 298 K and 353 K and variations of ε_r, γ , and G with temperature has been incorporated. The complexity of dependency on temperature comes from the fact that the shear modulus of the membrane is a function of temperature and also water content. Some experimental works showed that water can make the membrane stiffer or softer depending on the temperature [5]. Therefore, it is difficult to predict the impact of temperature on water uptake unambiguously.

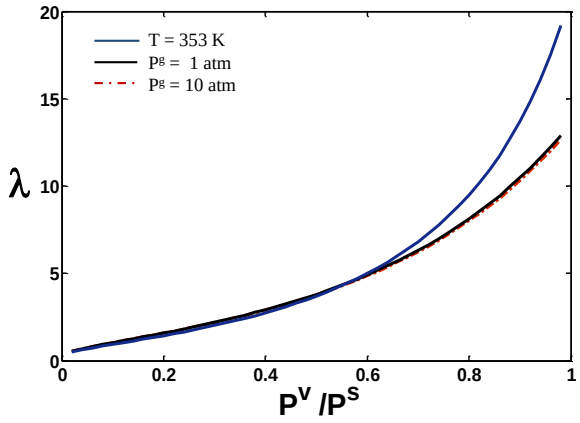

Figure 4.5: Effect of increase of temperature pressure on water sorption. Black line is the reference case with temperature 298 K and pressure of 1 atm. Blue line shows the impact of temperature at 353 K and dashed red line which is indistingushable from the reference case shows the effect of pressure at 10 atm.

4.2 Diagnostic Applications

In this section, we use the parameters in Table 3.1. The model links membrane water sorption and the evolution of the pore size distribution upon water uptake with the microscopic charge density distribution at pore surfaces and the microscopic shear modulus of hydrophobic polymer walls. Figure 4.6a shows the differential pore volume distribution at different RH values, for the reference case.

The model also allows calculating the microscopic statistical distribution of surface charges and elastic pressures. Figures 4.6a exhibits the differential pore volume as a function of pore radius at different RH values. Figure 4.6b shows the statistical pore density vs. elastic pressure. Upon increase of the RH, elastic pressures at the pore level shift to larger values. The statistical pore density distribution vs. elastic pressure becomes wider. Therefore, increasing water uptake results in a more heterogeneous pressure distribution in the PEM, which induces larger stress fluctuations and an increased propensity to mechanical degradation [42, 51].

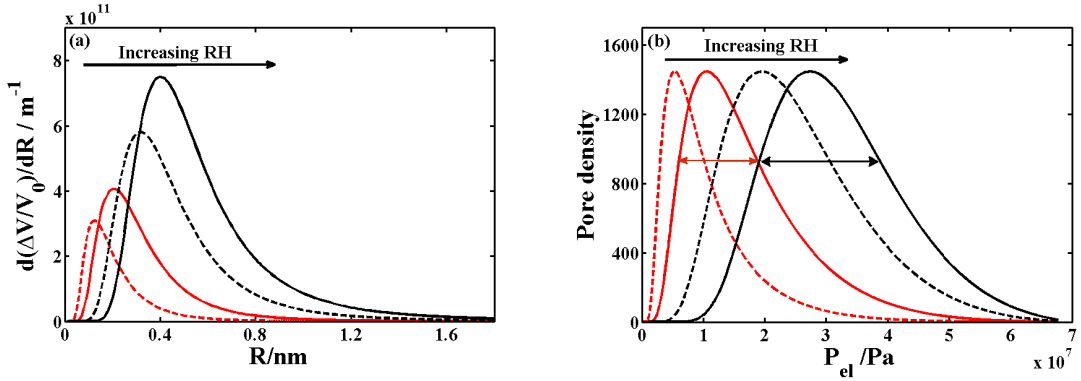

(a) (b)

Figure 4.6: (a) Differential pore volume as a function of pore radius of the ensemble upon increasing relative humidity (25%, 50%, 75% and 90%); (b) Statistical pore density distribution vs. elastic pressure upon increasing relative humidity (25%, 50%, 75% and 90%).

4.2.1 Membrane Degradation Analysis

As discussed earlier, due to the nature of the membrane, it suffers from performance degradation, leading to failure at times less than the required life time. It is commonly believed that the progressive deterioration of the membrane structure is caused by coupled chemical, mechanical and thermal mechanisms.

In this section, we use the model to discuss water sorption data of PEMs that have undergone structural changes. Based on this analysis, we infer a structural rationale for the observed changes in water sorption. We evaluated data sets from different experimental protocols, exploring the impact of hygrothermal aging and chemical degradation. We used the parameters in Table 3.1 as a reference state for fresh membranes.We kept $\bar{\sigma_0}$ and d_{σ_0} constant for chemical degradation studies because the change in IEC is small ($<$ 10 %). However, in case of hygrothermal aging, the average wall charge density of pores changed because of the drastic decrease in IEC. Finally, during degradation studies, G and α were considered as free parameters of the model that are adapted to best reproduce water sorption data. We used R-squared statistics in order to find the best value for these two parameters.

Collette *et al.* studied the hygrothermal stability of chemically stabilized solution-cast Nafion (NRE212CS) through monitoring changes in water sorption, conductivity, ion-exchange capacity and mechanical properties. A series of membrane samples were aged at 80^0C and 80% relative humidity in a climatic chamber [10]. Samples were regularly removed for analysis. During the aging test, the mass percentage of water uptake was observed to decrease along with the decreasing IEC, as shown in Figure 4.7a and 4.7b.

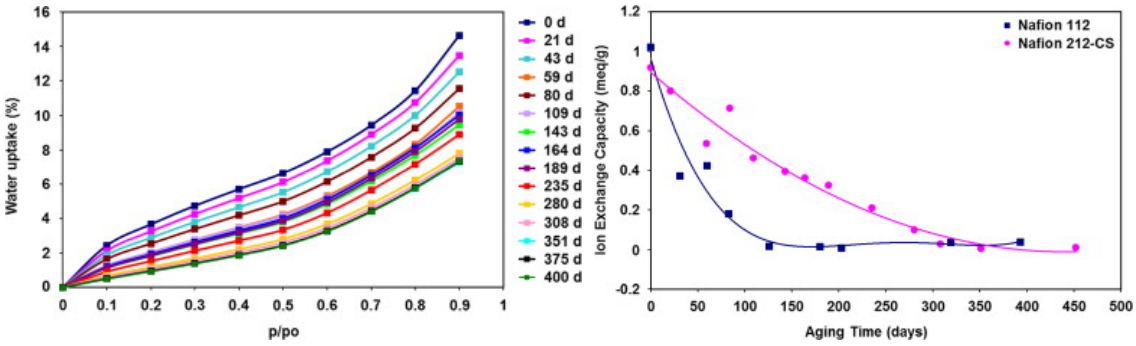

(a) (b)

Figure 4.7: a) Experimental water sorption isotherms of Nafion 212 recorded at 50 °C as a function of aging time [10] ; b) Membrane ion-exchange capacity for Nafion 112 and 212 as a function of aging time [10].

In another study, Luo *et al.* explored the chemical degradation of Nafion membranes via it*ex situ* testing with Fenton reagents (Fe^{2+}) in the presence of H_2O_2. They observed an increase in water uptake with a loss of acid head groups as illustrated in Figures 4.8a and 4.8b.

Figure 4.9a shows water sorption isotherms of Collette *et al.* after 0, 80, and 280 days of hygrothermal aging [10]. By comparison with the water sorption model, we determined the corresponding statistical pore density distribution vs. surface charge density, as shown in Figure 4.9b. Good agreement of the model with experimental data is achieved if in the course of aging the average surface charge density and the shear modulus of polymer walls increase as reported in Table 4.2. The total number of pores decreases drastically, as indicated by the area under the curve in Figure 4.9b. Moreover, reorganization of surface groups during swelling becomes more pronounced, as indicated by the value of α that increases upon aging. The increasing trend for the shear modulus is in agreement with experimental findings as shown in Table 4.2. In the study of Collette *et al.*, the mechanical properties were determined by tensile tests. Samples were equilibrated at least 24 h at 23°C and 50% RH prior to measurements. A stretching rate of 2.5 mm/min was applied after adjusting the zero stress for each sample. The reproducibility was checked by analysing 8 samples for each measurement and the experimental errors are 14 MPa on the Young modulus and 10% on the elongation at break [10].

As discussed in Ref. [64], PFSA ionomers assemble into bundles. During hygrothermal aging, the number of rods per bundle increases. The growth in equilibrium bundle size causes a stiffening of polymer walls. In this case, the growing core region of the typical bundle swallows a large fraction of ion exchange sites, explaining the dramatic decrease in IEC. At the same time, if we assume the length of side chains as being equal to twice the diameter of each rod, $l_{sc} \simeq 2d_R$, dissociated side

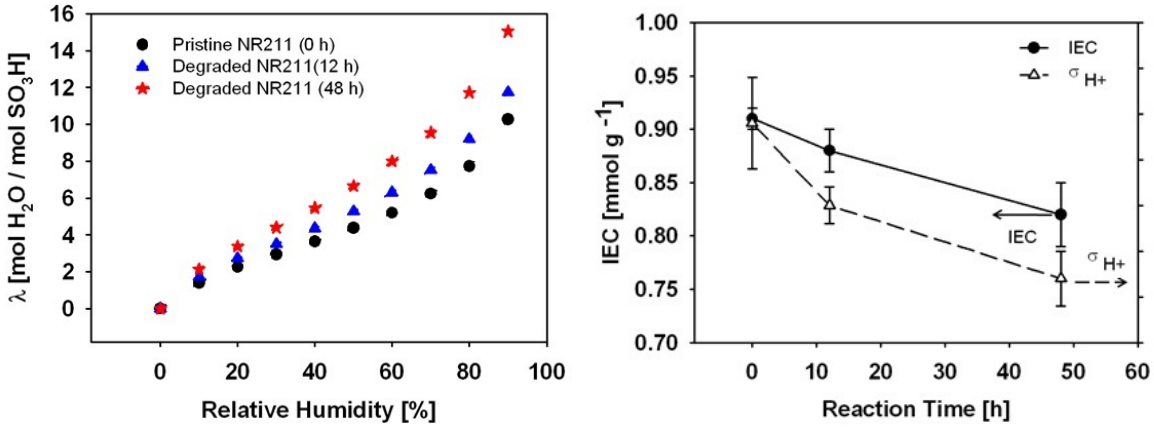

(a) (b)

Figure 4.8: a) Experimental water sorption isotherms of Nafion 211 recorded at 25°C as a function of aging time; b) Membrane ion-exchange capacity for Nafion 211 as a function of aging time.

chains from the second layer of rods in the bundle increase the effective surface charge density of bundles. This structural effect could explain the doubling of $\bar{\sigma_0}$, seen in Figure 4.9b. The evolution of bundle size and surface charge density is illustrated schematically in Figure 4.10. The total volumetric water uptake decreases because of the drastic reduction in the total number of pores. However, water uptake per solvated sulfonic acid group increases since each pore swells more strongly. The differential pore volume as a function of pore radius is shown in Figure 4.9c and the statistical pore density distribution vs. elastic pressure is presented in Figure 4.9d.

Time	**0**	**80**	**280**	**Days**
Microscopic shear modulus	380	480	520	MPa
Experimental macroscopic shear modulus	131	-	260	MPa
α	0.6	0.7	0.8	-

Table 4.2: Microscopic shear modulus, measured macroscopic shear modulus and degree of surface charge reorganization corresponding to the water sorption isotherms in Figure 4.9a. Experimental values are extracted from [10].

In the case of chemically degraded membranes, an irreversible decrease in ion exchange capacity of the membrane was observed, reproduced in Figure 4.11a. Water sorption isotherms taken after 0, 12 hours and 48 hours of degradation are shown in Figure 4.11b. Good agreement of the

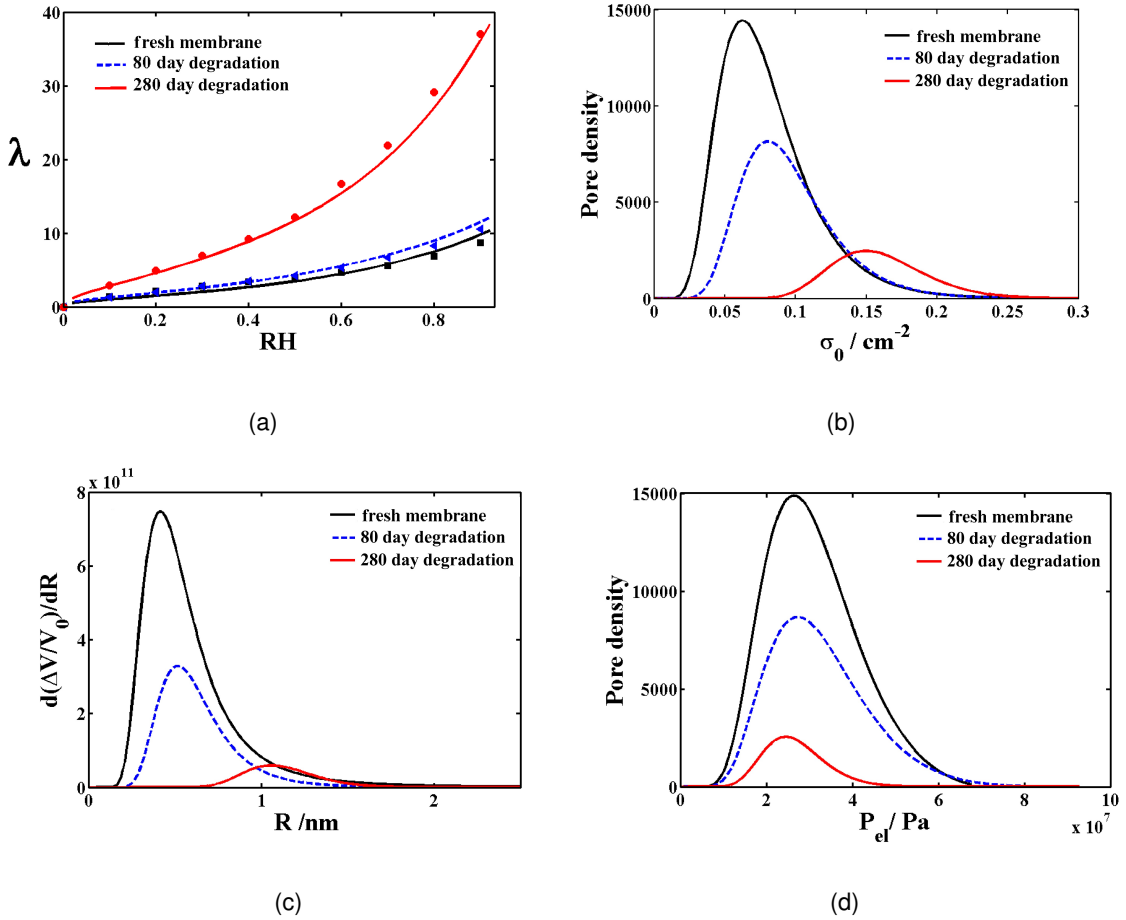

Figure 4.9: (a) Water sorption isotherms recorded in aging study after 0, 80 and 280 days [10], dots represent experimental data and lines correspond to curves calculated in the model. (b) Statistical pore density distribution vs. surface charge density corresponding to the water sorption isotherms in Figure 4.9a. (c) Differential pore volume as a function of pore radius corresponding to the water sorption isotherms in Figure 4.9a. (d) Statistical pore density distribution vs. elastic pressure, corresponding to the water sorption isotherms in Figure 4.9a.

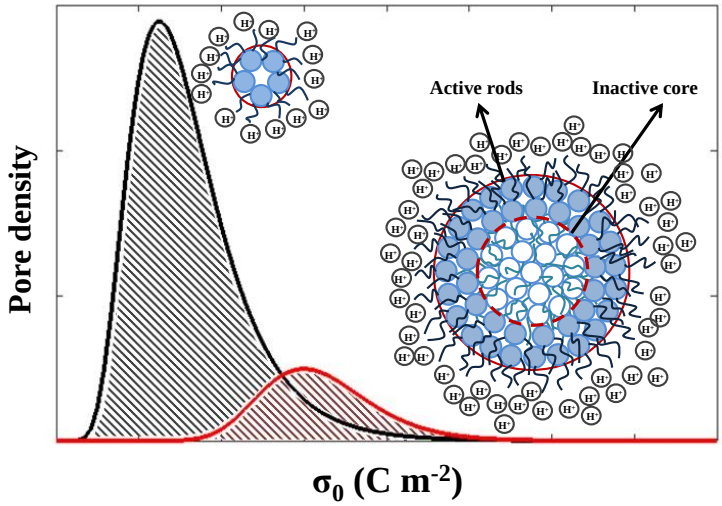

Figure 4.10: Evolution of bundle size and surface charge density upon aging. Cross-section of the bundle for a fresh membrane (left) and aged membrane (right). The total number of pores are indicated by the area under the curve.

model with experimental data is achieved if a loss of anionic surface groups, softening of the PEM, and a higher degree of surface group reorganization are considered, as reported in Table 4.3. As discussed in Ref. [64], the decrease of the surface charge density due to chemical degradation, seen in Figure 4.11b, is expected to result in smaller equilibrium bundle sizes and correspondingly reduced shear moduli. As a consequence, pores can swell to larger equilibrium radii, as seen in Figure 4.11c, while the elastic pressure distribution shifts to lower pressures, as exhibited in Figure 4.11d. As these examples show, the model is able to rationalize seemingly contradictory findings under aging and chemical degradation.

Time	**0**	**12**	**48**	**Hours**
Microscopic shear modulus	450	380	280	MPa
α	0.7	0.8	1.2	-

Table 4.3: Microscopic shear modulus and degree of surface charge reorganization corresponding to the water sorption isotherms in Figure 4.11b.

As these examples show, the model is able to rationalize structural changes caused by aging and chemical degradation that may seem contradictory at first sight.

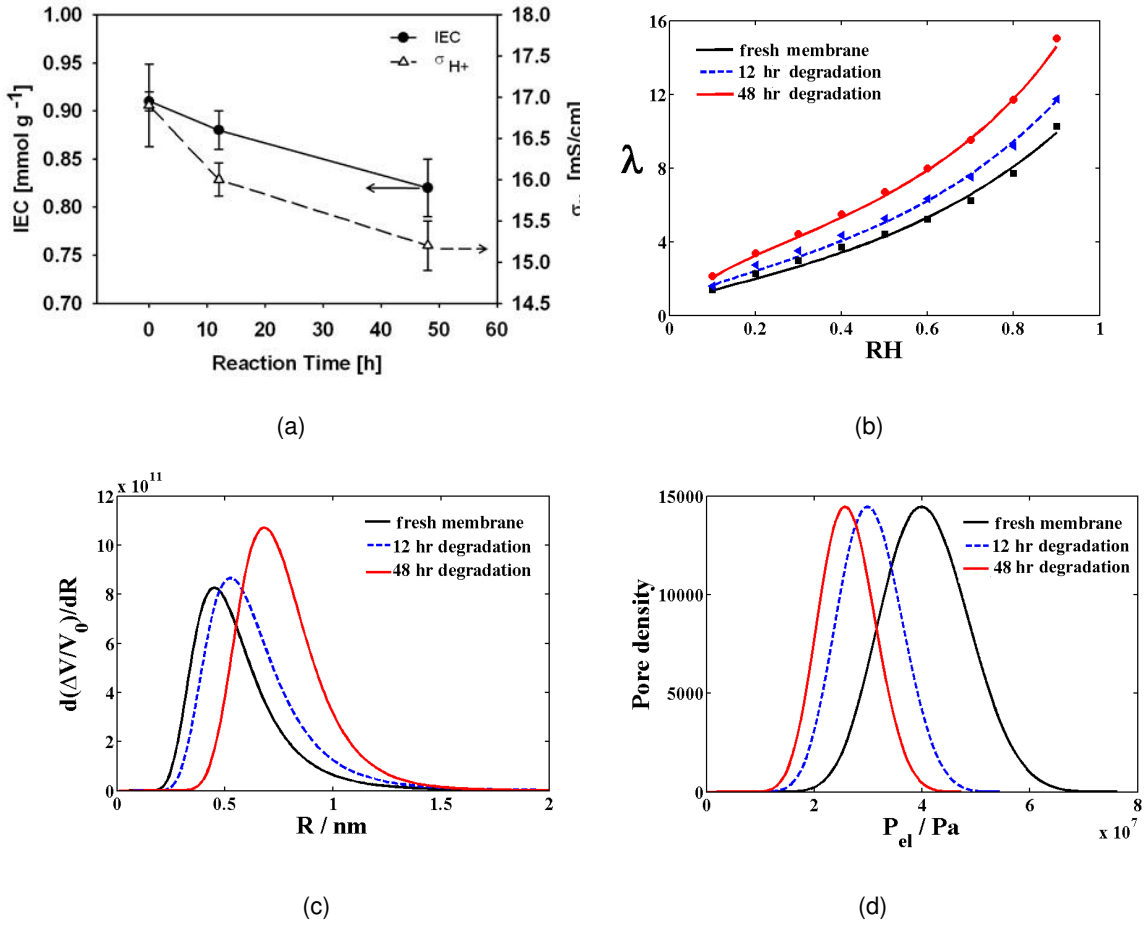

Figure 4.11: (a) Measured ion exchange capacity and proton conductivity of degrading PEMs. (b) Water sorption isotherms after 0, 12 and 48 hours of chemical degradation. (c) Differential pore volume as a function of pore radius, corresponding to the water sorption isotherms in Figure 4.11b. (d) Statistical pore density distribution vs. elastic pressure corresponding to the water sorption isotherms in Figure 4.11b. Experimental date have been generously give to us by Xiaoyan Luo and Steven Holdcroft for the use in this work.

Chapter 5

Summary and Conclusion

5.1 Conclusions and Future Work

This work expands on the poroelectroelastic model of water sorption in PEMs. The model rationalizes the sensitivity of water sorption to the density of anionic groups at pore walls. It accounts for the reorganization of anionic groups upon swelling, the dielectric properties of the solvent in pores, and the microscopic elastic properties of the polymer matrix. At the single pore level, the balance of pressures controls water sorption and swelling. This balance leads to the relation for the microscopic swelling parameter as a function of thermodynamic conditions and microscopic structure-related properties, including the density of anionic groups at pore walls, the dielectric permittivity of water in pores, and the shear modulus of polymer walls. The model reconciles microscopic swelling at the single pore level with macroscopic swelling effects in an ensemble of pores. The macroscopic volumetric expansion involves a convolution of single pore swelling, with the surface charge density distribution.

As discussed, pores have different sizes which lead to different elastic properties, surface charge density and radial fluctuation in the dielectric constant. Because of the complex interplay of membrane microstructure, reorganization upon swelling and effective material properties (ε, σ_0, G), along with their statistical fluctuations in a pore ensemble, it is elusive to reproduce quantitative predictions without ambiguity. This ambiguity was reduced in our model by a good choice of the probability distribution of the surface group density. We established the probability distribution function for surface charge density of pores for Nafion, which is the most common membrane for PEFC applications. A log normal distribution function was used to represent the statistical pore density distribution as a function of surface charge density. Using this distribution as input, the model was used to reproduce sorption isotherms for water. An improvement can be done by taking into account the correlation of

the statistical fluctuation of elastic modulus of the pore walls, dielectric properties as well as surface charge density.

The aforementioned mechanism for PEM water sorption is consistent with thermodynamic principles. It can also predict experimentally found trends correctly. Moreover, it is remarkable that by only changing the dielectric constant of the solvent, the model is capable of reproducing experimental alcohol sorption data.

Our model gives a statistical distribution of pore size and local stress in pores. In addition, a reverse analysis of water sorption isotherms of a given PEM type can provide the pore size distribution, and, further, the surface charge density distribution and statistical distribution of local stress in pores, which can not be obtained experimentally. Recently, the theory of bundle formation by Melchy and Eikerling provided sizes, electrostatic and elastic properties of ionomer bundles [64]. The merging point of this theory with our model will be the theory of fracture formation in charged polymer membranes. The formation and propagation of fractures determines the lifetime of materials. Specific challenges related to fracture formation in PEMs result from the interplay of elastic and osmotic effects and the presence of a fluctuating internal stress caused by water sorption. The latter point is illustrated in Figure 4.6b, which shows the statistical distribution of elastic pressure in pores. The elastic properties of ionomer bundles, including the local stress they experience, are, thus, subject to statistical fluctuations [18]. Moreover, considering defect formation and their impact on local mechanical properties as well as the effect of cycling will lead to a more realistic ageing model.

An insightful area of application of this model is the study of water sorption isotherms of PEMs that have undergone hygrothermal aging or chemical degradation. As demonstrated, this analysis relates trends in water uptake and swelling to changes in the size of ionomer bundles, bundle elasticity, surface charge density and reorganization of surface charges upon pore growth. Moreover, we obtained the statistical pore density distribution vs. elastic pressure at various water uptakes and under various aging and degradation protocols. Based on model calculations, upon hygrothermal aging, the average surface charge density and elastic modulus of polymer walls increases. At the same time, water uptake of the membrane increases while the IEC decreases dramatically. The calculated pore volume distribution results in a system with larger pores. We explained the contradictory observation of ”higher water uptake while having lower IEC and stiffer polymer walls” using the theory of bundle formation by Melchy and Eikerling [64]. In the case of chemical degradation, model calculation resulted in softening of PEM and higher degree of surface charge reorganization, which also can be explained by the Melchy and Eikerling’s bundle formation theory [64]. The presented analyses demonstrate that our water sorption model can be applied as a valuable diagnostic tool.

Despite several assumptions and simplifications that were needed to derive an analytical model, our model can capture all the physical properties and explain the thermodynamics of water sorption in PEMs. In order to further improve the model, we should revisit assumptions. In this study, the effective permittivity of water was assumed to be constant for pores with different sizes but the dielectric constant of water in the pore will increase with pore size. An increase of the effective permittivity leads to a lower osmotic pressure and consequently less steep water uptake at high RH. Assuming a modified Poisson-Boltzmann approach might be better suited to describe the electrostatic phenomena in such PEM pores.

One of the main important aspects of our model is the microscopic elastic properties. Here, we used an approximation in order to determine a relation between the microscopic deformation ratio and the macroscopic dimensional change of the membrane. The elastic properties of a bundle are explained in Ref. [64]. One should further develop this model to calculate elastic properties of the network of pores using the statistical distribution and a mean field approach. Moreover, mechanical properties at the microscopic scale still needs to be measured. Experiments for measurement of microscopic elastic modulus have been performed for biologically relevant systems, for example, for DNA systems. It would be useful to perform similar experiments in the PEM system. A comparison between these results and our model results would help in verifying our findings. Moreover, important insights for the development of PEM that are suitable for PEFCs application with longer life time can be gained.

Bibliography

[1] A. M. Affoune, A. Yamada, and M. Umeda. Conductivity and surface morphology of nafion membrane in water and alcohol environments. *J. power sources*, 148:9–17, 2005.

[2] J. Andjar and F. Segura. Fuel cells: History and updating. a walk along two centuries. *Renewable and Sustainable Energy Reviews*, 13(9):2309 – 2322, 2009.

[3] E. Antolini. The stability of lialo$_2$ powders and electrolyte matrices in molten carbonate fuel cell environment. *Ceram. Int.*, 39(4):3463–3478, 2013.

[4] S. Badwal and K. Foger. Solid oxide electrolyte fuel cell review. *Ceram. Int.*, 22(3):257–265, 1996.

[5] J. Benziger, A. Bocarsly, M. J. Cheah, P. Majsztrik, B. Satterfield, and Q. Zhao. Mechanical and transport properties of nafion: Effects of temperature and water activity. In *Fuel Cells and Hydrogen Storage*, pages 85–113. Springer, 2011.

[6] J. Bockris and S. Srinivasan. Fuel cells-their electrochemistry. 1969.

[7] M. Cappadonia, J. W. Erning, S. M. S. Niaki, and U. Stimming. Conductance of nafion 117 membranes as a function of temperature and water content. *Solid State Ionics*, 77:65–69, 1995.

[8] P. Choi and R. Datta. Sorption in proton-exchange membranes an explanation of schroeder's paradox. *J. Electrochem. Soc.*, 150(12):E601–E607, 2003.

[9] P. Choi, N. H. Jalani, and R. Datta. Thermodynamics and proton transport in nafion i. membrane swelling, sorption, and ion-exchange equilibrium. *J. Electrochem. Soc.*, 152(3):E84–E89, 2005.

[10] F. M. Collette, F. Thominette, H. Mendil-Jakani, and G. Gebel. Structure and transport properties of solution-cast nafion® membranes subjected to hygrothermal aging. *J. Membr. Sci.*, 435:242–252, 2013.

[11] A. Collier, H. Wang, X. Zi Yuan, J. Zhang, and D. P. Wilkinson. Degradation of polymer electrolyte membranes. *Int. J. Hydrogen Energy*, 31(13):1838–1854, 2006.

[12] D. E. Curtin, R. D. Lousenberg, T. J. Henry, P. C. Tangeman, and M. E. Tisack. Advanced materials for improved pemfc performance and life. *J. Power Sources*, 131(1):41–48, 2004.

[13] V. Detallante, D. Langevin, C. Chappey, M. Mtayer, R. Mercier, and M. Pinri. Water vapor sorption in naphthalenic sulfonated polyimide membranes. *J. Membr. Sci.*, 190(2):227 – 241, 2001.

[14] J. Divisek, M. H. Eikerling, V. Mazin, H. Schmitz, U. Stimming, and Y. M. Volfkovich. A study of capillary porous structure and sorption properties of nafion proton-exchange membranes swollen in water. *J. Electrochem. Soc.*, 145(8):2677–2683, 1998.

[15] R. Doshi, V. L. Richards, J. Carter, X. Wang, and M. Krumpelt. Development of solid-oxide fuel cells that operate at 500 °c. *J. Electrochem. Soc.*, 146(4):1273–1278, 1999.

[16] J. A. Dura, V. S. Murthi, M. Hartman, S. K. Satija, and C. F. Majkrzak. Multilamellar interface structures in nafion. *Macromolecules*, 42(13):4769–4774, 2009.

[17] M. H. Eikerling and P. Berg. Poroelectroelastic theory of water sorption and swelling in polymer electrolyte membranes. *Soft Matter*, 7(13):5976–5990, 2011.

[18] M. H. Eikerling and A. Kulikovsky. *Polymer Electrolyte Fuel Cells: Physical Principles of Materials and Operation*. CRC Press, 2014.

[19] M. H. Eikerling and K. Malek. Physical modeling of materials for pefcs: A balancing act of water and complex morphologies. In D. P. Wilkinson, J. Zhang, R. Hui, J. Fergus, and X. Li, editors, *Proton Exchange Membrane Fuel Cells: Materials, Properties and Performance*, pages 343–435. CRC Press, Boca Raton, 2009.

[20] M. H. Eikerling, Y. I. Kharkats, A. Kornyshev, and Y. M. Volfkovich. Phenomenological theory of electro-osmotic effect and water management in polymer electrolyte proton-conducting membranes. *J. Electrochem. Soc.*, 145(8):2684–2699, 1998.

[21] M. H. Eikerling, A. Kornyshev, A. Kuznetsov, J. Ulstrup, and S. Walbran. Mechanisms of proton conductance in polymer electrolyte membranes. *J. Phys. Chem. B*, 105(17):3646–3662, 2001.

[22] M. H. Eikerling, A. A. Kornyshev, and A. A. Kulikovsky. Physical modeling of fuel cells and their components. *Encyclopedia of electrochemistry*, 2007.

[23] M. H. Eikerling, A. A. Kornyshev, and E. Spohr. Proton-conducting polymer electrolyte membranes: Water and structure in charge. In *Fuel Cells I*, pages 15–54. Springer, 2008.

[24] G. J. Elfring and H. Struchtrup. Thermodynamics of pore wetting and swelling in nafion. *J. Membr. Sci.*, 315(1):125–132, 2008.

[25] M. Falk. An infrared study of water in perfluorosulfonate (nafion) membranes. *Can. J. Chem.*, 58(14):1495–1501, 1980.

[26] P. Flory, M. Gordon, and N. McCrum. Statistical thermodynamics of random networks [and discussion]. *Proc. R. Soc. A*, 351(1666):351–380, 1976.

[27] P. J. Flory. *Principles of Polymer Chemistry*. Cornell University Press, Ithaca, 1953.

[28] V. Freger. Elastic energy in microscopically phase-separated swollen polymer networks. *Polymer*, 43(1):71–76, 2002.

[29] V. Freger, E. Korin, J. Wisniak, and E. Korngold. Measurement of sorption in hydrophilic pervaporation: Sorption modes and consistency of the data. *J. Membr. Sci.*, 164(1):251–256, 2000.

[30] H. Freundlich and H. S. Hatfield. Colloid and capillary chemistry. 1926.

[31] M. Fujimura, T. Hashimoto, and H. Kawai. Small-angle x-ray scattering study of perfluorinated ionomer membranes. 1. origin of two scattering maxima. *Macromolecules*, 14(5):1309–1315, 1981.

[32] P. Futerko and I.-M. Hsing. Thermodynamics of water vapor uptake in perfluorosulfonic acid membranes. *J. Electrochem. Soc.*, 146(6):2049–2053, 1999.

[33] G. Gebel. Structural evolution of water swollen perfluorosulfonated ionomers from dry membrane to solution. *Polymer*, 41(15):5829–5838, 2000.

[34] G. Gebel and O. Diat. Neutron and x-ray scattering: Suitable tools for studying ionomer membranes. *Fuel Cells*, 5(2):261–276, 2005.

[35] G. Gebel and J. Lambard. Small-angle scattering study of water-swollen perfluorinated ionomer membranes. *Macromolecules*, 30(25):7914–7920, 1997.

[36] L. Ghassemzadeh and S. Holdcroft. Quantifying the structural changes of perfluorosulfonated acid ionomer upon reaction with hydroxyl radicals. *J. Am. Chem. Soc.*, 135(22):8181–8184, 2013.

[37] L. Ghassemzadeh, M. Marrony, R. Barrera, K. D. Kreuer, J. Maier, and K. Müller. Chemical degradation of proton conducting perflurosulfonic acid ionomer membranes studied by solid-state nuclear magnetic resonance spectroscopy. *J. Power Sources*, 186(2):334–338, 2009.

[38] L. Ghassemzadeh, K. D. Kreuer, J. Maier, and K. Muller. Chemical degradation of nafion membranes under mimic fuel cell conditions as investigated by solid-state nmr spectroscopy. *J. Phys. Chem. C*, 114(34):14635–14645, 2010.

[39] L. Ghassemzadeh, K. D. Kreuer, J. Maier, and K. Müller. Evaluating chemical degradation of proton conducting perfluorosulfonic acid ionomers in a fenton test by solid-state f nmr spectroscopy. *J. Power Sources*, 196(5):2490–2497, 2011.

[40] M. Ghelichi, P. É. A. Melchy, and M. H. Eikerling. Radically coarse-grained approach to the modeling of chemical degradation in fuel cell ionomers. *J. Phys. Chem. B*, 118(38):11375–11386, 2014.

[41] T. Gierke, G. Munn, and F. Wilson. The morphology in nafion perfluorinated membrane products, as determined by wide-and small-angle x-ray studies. *J.Polym. Sci., Part B: Polym. Phys.*, 19(11):1687–1704, 1981.

[42] M.-A. Goulet, R. M. Khorasany, C. De Torres, M. Lauritzen, E. Kjeang, G. G. Wang, and N. Rajapakse. Mechanical properties of catalyst coated membranes for fuel cells. *J. Power Sources*, 234:38–47, 2013.

[43] P. Grimes. Historical pathways for fuel cells. *Aerospace and Electronic Systems Magazine, IEEE*, 15(12):7–10, 2000.

[44] W. T. Grubb. Fuel cell, 1959. US Patent 2,913,511.

[45] A. Gruger, A. Régis, T. Schmatko, and P. Colomban. Nanostructure of nafion® membranes at different states of hydration: An ir and raman study. *Vib. Spectrosc.*, 26(2):215–225, 2001.

[46] G. M. Gusler and Y. Cohen. Equilibrium swelling of highly cross-linked polymeric resins. *Ind. Eng. Chem. Res.*, 33(10):2345–2357, 1994.

[47] J. Halim, F. Büchi, O. Haas, M. Stamm, and G. Scherer. Characterization of perfluorosulfonic acid membranes by conductivity measurements and small-angle x-ray scattering. *Electrochim. Acta*, 39(8):1303–1307, 1994.

[48] T. L. Hill. *An Introduction to Statistical Thermodynamics*. Addison-Wesley Educational Publishers Inc., New Jersey, 1960.

[49] C. Huang, K. Seng Tan, J. Lin, and K. Lee Tan. Xrd and xps analysis of the degradation of the polymer electrolyte in h_2 - o_2 fuel cell. *Chem. Phys. Lett.*, 371(1):80–85, 2003.

[50] A. Ioselevich, A. Kornyshev, and J. Steinke. Fine morphology of proton-conducting ionomers. *J. Phys. Chem. B*, 108(32):11953–11963, 2004.

[51] R. M. Khorasany, M.-A. Goulet, A. S. Alavijeh, E. Kjeang, G. G. Wang, and R. Rajapakse. On the constitutive relations for catalyst coated membrane applied to in-situ fuel cell modeling. *J. Power Sources*, 252:176–188, 2014.

[52] A. Kongkanand. Interfacial water transport measurements in nafion thin films using a quartz-crystal microbalance. *J. Phys. Chem. C*, 115(22):11318–11325, 2011.

[53] K. D. Kreuer. On the development of proton conducting materials for technological applications. *Solid State Ionics*, 97(1):1–15, 1997.

[54] K. D. Kreuer. On the development of proton conducting polymer membranes for hydrogen and methanol fuel cells. *J. Membr. Sci.*, 185(1):29–39, 2001.

[55] K. D. Kreuer and G. Portale. A critical revision of the nano-morphology of proton conducting ionomers and polyelectrolytes for fuel cell applications. *Adv. Funct. Mater.*, 23(43):5390–5397, 2013.

[56] A. Kusoglu, M. H. Santare, and A. M. Karlsson. Mechanics-based model for non-affine swelling in perfluorosulfonic acid (pfsa) membranes. *Polymer*, 50(11):2481–2491, 2009.

[57] Y. Li, Q. T. Nguyen, C. L. Buquet, D. Langevin, M. Legras, and S. Marais. Water sorption in nafion® membranes analyzed with an improved dual-mode sorption modelstructure/property relationships. *J. Membr. Sci.*, 439:1–11, 2013.

[58] S. Lyonnard and G. Gebel. Neutrons for fuel cell membranes: Structure, sorption and transport properties. *Eur. Phys. J.*, 213(1):195–211, 2012.

[59] B. MacMillan, A. R. Sharp, and R. L. Armstrong. Nmr relaxation in nafion the low temperature regime. *Polymer*, 40(10):2481–2485, 1999.

[60] H. Magnet. Handbook of fuel cell technology-c. berger, 1968.

[61] L. Maldonado, J.-C. Perrin, J. Dillet, and O. Lottin. Characterization of polymer electrolyte nafion membranes: Influence of temperature, heat treatment and drying protocol on sorption and transport properties. *J. Membr. Sci.*, 389:43–56, 2012.

[62] K. A. Mauritz and R. B. Moore. State of understanding of nafion. *Chem. Rev.*, 104(10): 4535–4586, 2004.

[63] K. A. Mauritz and C. Rogers. A water sorption isotherm model for ionomer membranes with cluster morphologies. *Macromolecules*, 18(3):483–491, 1985.

[64] P. E. A. Melchy and M. H. Eikerling. Physical theory of ionomer aggregation in water. *Phys. Rev. E*, 89:032603, 2014.

[65] M. M. Mench. *Fuel cell engines*. John Wiley & Sons, 2008.

[66] M. V. Mirkin. Peer reviewed: Recent advances in scanning electrochemical microscopy. *Anal. Chem.*, 68(5):177A–182A, 1996.

[67] C. C. Mitigation. Ipcc special report on renewable energy sources and climate change mitigation. 2011.

[68] M. A. Modestino, A. Kusoglu, A. Hexemer, A. Z. Weber, and R. A. Segalman. Controlling nafion structure and properties via wetting interactions. *Macromolecules*, 45(11):4681–4688, 2012.

[69] J. Musty, R. Pattle, and P. Smith. The swelling of rubber in liquid and vapour (schroeder's paradox). *J. Appl. Chem.*, 16(8):221–222, 1966.

[70] D. Nandan, B. Venkataramani, and A. Gupta. Ionic hydration and water sorption isotherms of ion exchange resins. *Langmuir*, 9(7):1786–1793, 1993.

[71] K. A. Page, A. Kusoglu, C. M. Stafford, S. Kim, R. J. Kline, and A. Z. Weber. Confinement-driven increase in ionomer thin-film modulus. *Nano Lett.*, 14(5):2299–2304, 2014.

[72] R. Paul and S. J. Paddison. A statistical mechanical model for the calculation of the permittivity of water in hydrated polymer electrolyte membrane pores. *J. Chem. Phys.*, 115(16):7762–7771, 2001.

[73] S. Peighambardoust, S. Rowshanzamir, and M. Amjadi. Review of the proton exchange membranes for fuel cell applications. *Int. J. Hydrogen Energ.*, 35(17):9349–9384, 2010.

[74] J.-C. Perrin, S. Lyonnard, and F. Volino. Quasielastic neutron scattering study of water dynamics in hydrated nafion membranes. *J. Phys. Chem. C*, 111(8):3393–3404, 2007.

[75] A. M. Pivovar and B. S. Pivovar. Dynamic behavior of water within a polymer electrolyte fuel cell membrane at low hydration levels. *J. Phys. Chem. B*, 109(2):785–793, 2005.

[76] A. Pozio, R. Silva, M. De Francesco, and L. Giorgi. Nafion degradation in pefcs from end plate iron contamination. *Electrochim. Acta*, 48(11):1543–1549, 2003.

[77] D. Rivin, C. Kendrick, P. Gibson, and N. Schneider. Solubility and transport behavior of water and alcohols in nafion. *Polymer*, 42(2):623 – 635, 2001.

[78] D. Rivin, C. Kendrick, P. Gibson, and N. Schneider. Solubility and transport behavior of water and alcohols in nafion. *Polymer*, 42(2):623–635, 2001.

[79] E. Roche, M. Pineri, R. Duplessix, and A. Levelut. Small-angle scattering studies of nafion membranes. *J.Polym. Sci., Part B: Polym. Phys.*, 19(1):1–11, 1981.

[80] A. Roudgar, S. Narasimachary, and M. H. Eikerling. Hydrated arrays of acidic surface groups as model systems for interfacial structure and mechanisms in pems. *J. Phys. Chem. B*, 110 (41):20469–20477, 2006.

[81] A. Roudgar, S. Narasimachary, and M. H. Eikerling. Ab initio study of surface-mediated proton transfer in polymer electrolyte membranes. *Chem. Phys. Lett.*, 457(4):337–341, 2008.

[82] L. Rubatat, A. L. Rollet, G. Gebel, and O. Diat. Evidence of elongated polymeric aggregates in nafion. *Macromolecules*, 35(10):4050–4055, 2002.

[83] L. Rubatat, G. Gebel, and O. Diat. Fibrillar structure of nafion: Matching fourier and real space studies of corresponding films and solutions. *Macromolecules*, 37(20):7772–7783, 2004.

[84] M. Rubinstein, R. H. Colby, A. V. Dobrynin, and J.-F. Joanny. Elastic modulus and equilibrium swelling of polyelectrolyte gels. *Macromolecules*, 29(1):398–406, 1996.

[85] D. A. Schiraldi. Perfluorinated polymer electrolyte membrane durability. *J. Macromolecular Sci., Part C: Poly. Rev.*, 46(3):315–327, 2006.

[86] K. Schmidt-Rohr and Q. Chen. Parallel cylindrical water nanochannels in nafion fuel-cell membranes. *Nat. Mater.*, 7(1):75–83, 2008.

[87] L. M. Schwartz, S. Feng, M. Thorpe, and P. N. Sen. Behavior of depleted elastic networks: Comparison of effective-medium and numerical calculations. *Phys. Rev. B*, 32(7):4607–4617, 1985.

[88] A. Shah, T. Ralph, and F. Walsh. Modeling and simulation of the degradation of perfluorinated ion-exchange membranes in pem fuel cells. *J. Electrochem. Soc.*, 156(4):B465–B484, 2009.

[89] N. Shaigan, W. Qu, D. G. Ivey, and W. Chen. A review of recent progress in coatings, surface modifications and alloy developments for solid oxide fuel cell ferritic stainless steel interconnects. *J. Power Sources*, 195(6):1529–1542, 2010.

[90] Z. Siroma, R. Kakitsubo, N. Fujiwara, T. Ioroi, S.-i. Yamazaki, and K. Yasuda. Depression of proton conductivity in recast nafion® film measured on flat substrate. *J. Power Sources*, 189 (2):994–998, 2009.

[91] B. Smitha, S. Sridhar, and A. Khan. Solid polymer electrolyte membranes for fuel cell applications a review. *J. Membr. Sci*, 259(1):10–26, 2005.

[92] T. E. Springer, T. Zawodzinski, and S. Gottesfeld. Polymer electrolyte fuel cell model. *J. Electrochem. Soc.*, 138(8):2334–2342, 1991.

[93] Y. Volfkovich, V. Bagotzky, V. Sosenkin, and I. Blinov. The standard contact porosimetry. *Colloids Surf., A*, 187188(0):349 – 365, 2001.

[94] F. Volino, J.-C. Perrin, and S. Lyonnard. Gaussian model for localized translational motion: Application to incoherent neutron scattering. *J. Phys. Chem. B*, 110(23):11217–11223, 2006.

[95] E. D. Wachsman and K. T. Lee. Lowering the temperature of solid oxide fuel cells. *Science*, 334(6058):935–939, 2011.

[96] M. Wakizoe, O. A. Velev, and S. Srinivasan. Analysis of proton exchange membrane fuel cell performance with alternate membranes. *Electrochim. Acta*, 40(3):335–344, 1995.

[97] Y. Wang, Y. Kawano, S. R. Aubuchon, and R. A. Palmer. Tga and time-dependent ftir study of dehydrating nafion-na membrane. *Macromolecules*, 36(4):1138–1146, 2003.

[98] Y. Wang, K. S. Chen, J. Mishler, S. C. Cho, and X. C. Adroher. A review of polymer electrolyte membrane fuel cells: Technology, applications, and needs on fundamental research. *Appl. Energ.*, 88(4):981–1007, 2011.

[99] A. Z. Weber and J. Newman. Transport in polymer-electrolyte membranes i. physical model. *J. Electrochem. Soc.*, 150(7):A1008–A1015, 2003.

[100] A. Z. Weber and J. Newman. Transport in polymer-electrolyte membranes ii. mathematical model. *J. Electrochem. Soc.*, 151(2):A311–A325, 2004.

[101] J. Wing and D. Carter. The fuel cell today industry review 2013. *Corporate report, www. fuelcelltoday. com*, 2013.

[102] L. K. Wolff and E. Büchner. Über das schroedersche paradoxon. *Z. phys. Chem*, 89:271, 1915.

[103] J. Xie, D. L. Wood, D. M. Wayne, T. A. Zawodzinski, P. Atanassov, and R. L. Borup. Durability of pefcs at high humidity conditions. *J. Electrochem. Soc.*, 152(1):A104–A113, 2005.

[104] T. A. Zawodzinski, C. Derouin, S. Radzinski, R. J. Sherman, V. T. Smith, T. E. Springer, and S. Gottesfeld. Water uptake by and transport through nafion® 117 membranes. *J. Electrochem. Soc.*, 140(4):1041–1047, 1993.

[105] T. A. Zawodzinski, T. E. Springer, J. Davey, R. Jestel, C. Lopez, J. Valerio, and S. Gottesfeld. A comparative study of water uptake by and transport through ionomeric fuel cell membranes. *J. Electrochem. Soc.*, 140(7):1981–1985, 1993.

[106] T. A. Zawodzinski Jr, M. Neeman, L. O. Sillerud, and S. Gottesfeld. Determination of water diffusion coefficients in perfluorosulfonate ionomeric membranes. *J. Phys. Chem.*, 95(15): 6040–6044, 1991.

[107] Q. Zhao, N. Carro, H. Y. Ryu, and J. Benziger. Sorption and transport of methanol and ethanol in h^+-nafion. *Polymer*, 53(6):1267–1276, 2012.

[108] X. Zhao, W. Hong, and Z. Suo. Inhomogeneous and anisotropic equilibrium state of a swollen hydrogel containing a hard core. *Appl. Phys. Lett.*, 92(5):051904–051904, 2008.

[109] C. Zhou, M. A. Guerra, Z.-M. Qiu, T. A. Zawodzinski, and D. A. Schiraldi. Chemical durability studies of perfluorinated sulfonic acid polymers and model compounds under mimic fuel cell conditions. *Macromolecules*, 40(24):8695–8707, 2007.